Journal of Radioanalytical and Nuclear Chemistry (2024) 333:5025–5048
https://doi.org/10.1007/s10967-024-09667-4

Efficient adsorption of thorium and cerium from Rosetta monazite concentrate using a novel phosphorylated Schiff-base adsorbent

Mohamed A. Gado[1]

Received: 6 May 2024 / Accepted: 15 July 2024 / Published online: 7 August 2024
© The Author(s) 2024

Abstract
(Pyridine-2,5-diylbis(azaneylylidene)) bis-(methaneylylidene)) bis(benzene-5,1,3-triyl) tetrakis (hydrogen phosphonate) (PZMB) was successfully synthesized for Th(IV) and Ce(IV) adsorption, the adsorption parameters evaluated and found to be pH 3.5, time 60 min, dose 0.15 g. Adsorption kinetics, isotherm, and thermodynamics studies. Adsorption kinetics studies show that adsorbent follow pseudo-second-order model while isotherm studies conclude that adsorption processes fitted Langmuir and D-R isotherm model. The maximum adsorption capacity of BZMB of Th(IV) and Ce(IV) are 366.4 and 244.53 mg/g respectively, Thermodynamic studies indicate both adsorption processes exhibited by the PZMB were endothermic, spontaneous and sorption occurs in a random manner.

Keywords Thorium adsorption · Cerium adsorption · Phosphorylated Schiff base · Schiff base · Rare earth element

Introduction

Rare earth elements (REEs) possess a broad spectrum of applications, making them exceedingly valuable in various industries. For instance, alloys made from rare earth compounds, especially cerium, are employed in the entertainment industry to create carbon arc lighting for movie projectors and studio lighting. This application takes advantage of the compounds' ability to emit light closely resembling sunlight's spectrum, enhancing visual brightness and quality [1]. In the automotive sector, Toyota's hybrid model, the Prius, showcases innovation by using a nickel-lanthanum hydride battery, a departure from traditional lead-acid batteries. This development represents a stride towards more efficient energy storage technologies [2]. In the realm of nuclear energy, thorium is being explored as a potential alternative to uranium in fuel cycles. The interest in thorium lies in its capability to manage transuranic elements, such as plutonium, more effectively and to serve as an alternative fuel source, offering a safer and potentially more sustainable approach to nuclear energy production [3].

Thorium has shown promise as a source of alpha emitters, particularly 213Bi and 225Ac, which are being extensively researched for their potential in clinical applications to treat various types of cancer. The focus of this research is on the utilization of the short-range alpha particles emitted by 213Bi. These particles have the capability to goal and destroy cancer cells while minimizing damage to healthy surrounding tissues, making them a valuable tool in the fight against cancer [4].

Cerium, a key component of mischmetal alloys that can contain up to 50% cerium, is widely utilized in cigarette lighter flints due to its ability to generate sparks upon friction. This rare earth element also acts a vital role in the manufacturing of stainless steel and permanent magnets, serving as a precipitation hardening agent to enhance their properties. Moreover, cerium-based catalytic converters are instrumental in reducing vehicular emissions by converting nitrogen oxides and other pollutants into harmless nitrogen gas. Its application extends to the production of flat TV screens and low-energy light bulbs, including floodlights, highlighting its versatility and importance across various industries [5]. Given the critical roles of valuable rare earth elements (REEs) in such diverse applications, disregarding waste materials containing these metals is impractical. Consequently, developing efficient recycling methods is imperative to facilitate the recovery and reuse of these

✉ Mohamed A. Gado
mag.nma@yahoo.com

[1] Nuclear Materials Authority, 530, Maadi, Cairo, Egypt

vital resources, ensuring their sustainable management and conservation.

Monazite, a mineral abundant in thorium, uranium, and other rare earth elements (REEs), serves as a significant resource for these crucial materials. The extraction and, where feasible, separation of thorium, its associated REEs, and uranium are essential steps for their utilization in nuclear industry processes. Thorium reserves are more abundant in nature compared to uranium, offering a promising alternative for nuclear fuel. Currently, uranium is the predominant fuel for the majority of nuclear reactors globally. However, the focus is gradually shifting towards thorium reactors, which are viewed as a viable and potentially more sustainable option for the nuclear energy sector in the foreseeable future [6].

Various procedures have been planned for the recovery of thorium and cerium, highlighting the significance of these elements in numerous applications. Methods for instance solvent extraction, electro-flotation, reverse osmosis, ion exchange, sorption, and chemical precipitation have been investigated for their effectiveness in separating these valuable metals from their sources. Among these, adsorption stands out due to its affordability, simplicity, and environmental friendliness, making it an attractive alternative to more traditional separation techniques. This process involves the binding of ions or molecules to the active sites on sorbents, a mechanism that has been extensively researched [7–10]. Experiments have been conducted using both synthetic and naturally derived adsorbents to study the adsorption of thorium and cerium, aiming to achieve selective separation of these metal ions. Critical factors influencing the adsorption process include the sort of functional groups, sensitivity to pH changes, the degree of ionization (ability to donate or accept protons), and the structural characteristics of the sorbent's backbone. These parameters have an critical role in significant the selectivity and efficiency of the adsorption method [11].

The extraction of thorium and cerium from it's solutions has been discovered using a range of adsorbents, demonstrating the ongoing efforts to refine this process [12–15]. Among the myriad of adsorbents tested, those composed of organic molecules featuring nitrogen, oxygen, phosphorus, and sulfur atoms have shown to be particularly effective. A notable area of interest lies in the potential of complexes formed between Schiff bases, with the general formula RC=NR', and transition metal ions to act as efficient adsorbents. The effectiveness of Schiff bases as adsorbents is largely attributed to their ability to engage in electrostatic attraction with metal ions. This interaction is facilitated by the π-electron pairs and unshared electron pairs present in the Schiff bases, making them exceptionally promising candidates for the eliminate of metal ions from aqueous medium. This characteristic highlights the potential of Schiff bases in environmental cleanup and resource recovery applications, offering a promising avenue for the effectual and careful extraction of valuable metals like thorium and cerium from liquid mediums.

Schiff base sorbents, especially those rich in donor atoms like nitrogen (N) and oxygen (O), are renowned for their remarkable selectivity towards metal ions and their substantial adsorption capacities. The mechanism underlying this efficiency is the coordination between metal ions and Schiff base ligands, which facilitates the selective adsorption of specific metal ions. This unique property has been exploited in various forms of Schiff-based adsorbents, showcasing the versatility and effectiveness of these materials in metal ion recovery. Examples include poly (methyl vinyl ether-alt-maleic anhydride) that has been functionalized with a Schiff base [16], Schiff bases integrated into magnetic materials [17], alumina coated with sodium dodecyl sulfate and subsequently improved with a Schiff base [18], and mesoporous silica SBA-15 functionalized with Schiff base ligands [19]. Each of these innovations represents an advancement in the field of adsorption technology, offering tailored solutions for the efficient and selective removal of metal ions from aqueous solutions, thereby highlighting the critical role of Schiff base adsorbents in environmental remediation and resource recovery efforts.

The primary purpose of this study is to formulate a Schiff base derivative known as PZMB, designed to exhibit superior sorption capacity and efficiency as an adsorbent material. PZMB was meticulously evaluated through a series of analytical methods, containing mass spectrometry, FTIR, ^{1}H-NMR, ^{13}C-NMR, BET and ^{31}P-NMR. These evaluations were aimed at determining its capability to selectively extract lanthanides, specifically Ce (IV) and Th (IV), from Monazite leach liquor. The study extensively investigated the isotherms and kinetics of the sorption process, also the factors controlling as contact time, initial concentration, pH, temperature and adsorbent dosage. This research endeavors to pioneer an innovative adsorbent technology for the efficient separation of pure cerium and thorium from Rosetta monazite sand, and offering potential advancements in the utilization of REEs.

Experimental

Theoretical aspects

The process of extracting rare earth elements from monazite sands involves digesting the sands with hot sulfuric acid. This chemical reaction is pivotal for the production of a monazite sulfate paste, which contains rare earths along with residual silica, zircon, and other gangue minerals. The specific reaction can be described as follows (Eq. 1):

$$2REPO_4 + 3H_2SO_4 \rightarrow (RE)_2(SO_4)_3 + 2H_3PO_4 \quad (1)$$

This reaction results in the formation of a thick grey paste. Upon cooling, this paste is meticulously diluted with water to a volume approximately ten times that of the original mineral weight. Continuous stirring for at least 1 h is essential during this dilution process. The purpose of this procedure is to separate silica, rutile, zircon, and any unreacted monazite from the rare earth elements, effectively putting the latter into solution. This step is crucial for isolating the valuable rare earth elements from the mixture, facilitating their subsequent recovery and use.

Materials and methods

The research ensured analytical purity for all materials used. Ultrapure water, obtained through a Human Power-I system, and adjustments to solution pH levels with NaOH and HNO_3, underscored the meticulous preparation standards. To estimate the sorption levels of Th(IV) and Ce(IV), two pivotal instruments were employed: the Meterch Inc. SP-8001 spectrophotometer, which spans the UV to visible spectrum range of 200 to 1100 nm with a wavelength accuracy of ± 1 nm, and the PerkinElmer Optima: 2000 DV model ICP-OES, designed for precise ion quantification.

For structural analysis of monazite oxide cake, XRF spectrometry was conducted using a Panalytical Empyrean system, highlighting the detailed composition examination. Morphological insights were gained through the PHILIPS XL-30S FESEM Field Emission Scanning Electron Microscope, providing high-resolution images of the adsorbents. Lastly, the surface areas were measured employing the Brunauer–Emmett–Teller (BET) technique with a Micromeritics ASAP 2010, ensuring a comprehensive evaluation of the adsorbents' physical properties essential for effective Th(IV) and Ce(IV) adsorption.

In the course of this study, analytical grade chemicals were used to ensure the purity of all chemical components. To adjust the pH levels of solutions, (NaOH) and (HNO_3) were employed, while ultrapure water was obtained from the Human Power-I system. The quantification of thorium (Th(IV)) and cerium (Ce(IV)) adsorption remaining in the solution was carried out using a spectrophotometer (Meterch Inc. SP-8001). This spectrophotometer is a single beam instrument capable of covering both the UV and visible spectrum ranges from 200 to 1100 nm, with a wavelength accuracy of ± 1 nm. Additionally, Inductively Coupled Plasma Optical Emission Spectrometry (ICP-OES) was utilized, specifically the PerkinElmer Optima: 2000 DV model, for precise measurement of these ions.

For analyzing the structural composition of monazite oxide cake, X-ray fluorescence (XRF) spectrometry was used, employing a Panalytical Empyrean system with a wavelength of 1.54 Å. The morphology of the materials was examined using a Field Emission Scanning Electron Microscope (Model: PHILIPS XL-30S FESEM), providing detailed images of the adsorbents' surfaces. Surface area measurements were conducted using the Brunauer, Emmett, and Teller (BET) technique, facilitated by a Micromeritics ASAP 2010 instrument. This comprehensive suite of analytical techniques ensured a thorough examination of the adsorbent's performance and characteristics, contributing to the detailed understanding of their capabilities in adsorbing Th(IV) and Ce(IV) ions from solutions.

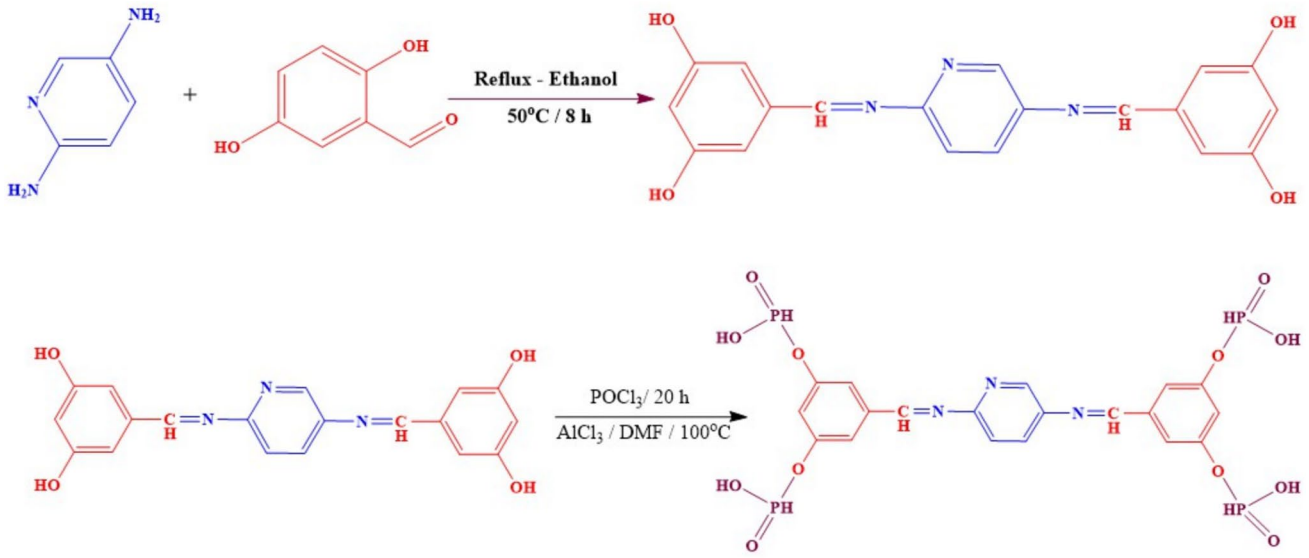
Chemicals

The chemicals utilized in this study were sourced from various Chinese companies, ensuring that each compound met the requisite analytical quality standards without the need for further purification. Specifically, the 3, 5-dihydroxybenzaldehyde was supplied by Shanghai Macklin Biochemical Co., Ltd., highlighting the importance of high-quality starting materials for the synthesis processes. Ethanol, essential for various procedural steps, was obtained from Sinopharm Chemical Reagent Co., Ltd. The critical components, 2,6-diamine pyridine (DP), sodium hydroxide, and aluminum chloride ($AlCl_3$), were all provided by Shanghai Aladdin Reagent Co., Ltd., ensuring consistency in the reagents used. Additionally, DMF and $POCl_3$, crucial for specific synthesis reactions, were acquired from Sichuan Xilong Scientific Co., Ltd.

Preparation of PZMB adsorbent

3,5-dihydroxybenzaldehyde (0.04 mol, 5.52 g) dissolved in ethanol (25 mL) is added slowly drop by drop to a solution of pyridine-2,6-diamine (PD) (0.02 mol, 2.2 g) dissolved in 25 ml of warm ethanol (50 °C). The mixture was refluxed with continuous stirring for 8 h to allow for complete precipitation. orange-yellow precipitate of (5,5′-((pyridine-2,5-diylbis (azaneylylidene)) bis(methaneylylidene)) bis(benzene-1,3-diol)) [ZMB] was attained. The attained precipitate was next filtered off, rained with ethyl alcohol (C_2H_5OH)several times, dried in a vacuum desiccator.

Synthetic ZMB (1 g), and 0.15 g of $AlCl_3$ (anhydrous) were refluxed with 20 mL of phosphorus oxychloride in DMF for complete phosphorylation process for 20 h at 100 °C, with the presence of tail gas absorber to adsorb any HCl release during the process [20–22]. Once that was done, of distilled water 200 mL was additional to the blend very gradually over the course of a few minutes while it was sitting in an ice bath. The obtained dark yellow product of ((pyridine-2,5-diylbis(azaneylylidene)) bis-(methaneylylidene))bis(benzene-5,1,3-triyl) tetrakis



Scheme 1 Flow sheet of the preparation of ZMB and PZMB adsorbent

(hydrogen phosphonate) (PZMB) washed several times with absolute C_2H_5OH, then dried for 12 h at 80 °C, Scheme 1.

Monazite stock solution preparation

In this study, Rositta Monazite sand served as the source material for the monazite sand sample. The experimental procedure began with the digestion of 100 g of monazite sand, which had a purity of 70%, in 300 ml of 80% sulfuric acid. This mixture was subjected to heating at 180 °C for approximately 3 h, followed by stirring for 1–2 h to ensure thorough mixing. After the digestion process, the white slurry was diluted with two liters of cold water and subsequently filtered to solid liquid separation. The final stage involved transferring the white oxalate precipitate to a calciner, where it was heated at 500 °C for 2 h.

To precipitate thorium and the REE s (total) as oxalate cakes, the filtrate's pH was carefully adjusted to a range of 1.1–1.5. Following this pH adjustment, a 10% $C_2H_2O_4$ (oxalic acid) solution was supplementary to the mixture. After the addition of ($C_2H_2O_4$), the resulting precipitate was permissible to settle for 6 h. This step is crucial as oxalic acid reacts with the dissolved metals to form insoluble oxalates, effectively separating them from the solution. To remove any remaining impurities and to purify the precipitate, it was washed several times with a 2% oxalic acid solution. The use of oxalic acid in the washing process helps to dissolve any non-oxalate impurities while leaving the oxalate precipitate complete. After washing with oxalic acid, the precipitate was further rinsed with distilled water. This final washing step is critical to remove any residual oxalic acid and to ensure that the oxalate cakes are as pure as possible, ready for subsequent treatment or analysis, after which the calcination process was converting the oxalate forms of thorium and rare earth elements into their oxide forms [23].

The chemical composition of working sulfate leach liquor of Rosetta monazite concentrate 2.358 g/L Th, 0.371 g/L U, 200.12 g/L, 32.20 g/L REE, SO_4^{2-}, 8.94 g/L, PO_4^{3-}, 1.26 g/L SiO_2, 0.28 g/L CaO, 0.23 g/L Fe_2O_3 and 0.12 g/L TiO_2; These conditions included a concentration of 80% sulfuric acid and a solid/liquid ratio of 1:3. The process was conducted over a duration of 2.5 h at a maintained temperature of 180 °C. Before its dissolution in nitric acid, the oxide cake of Monazite underwent detailed analysis using (XRF) and (ICP) to determine its elemental composition. The concentrations of various elements within the cake, with the results documented in Table 1. Following the calcination process, the oxide cake was liquified in 1 L of 8 M HNO_3, resulting in a nitrate stock solution. This solution was found to contain thorium (Th(IV)) at a concentration of 2793 parts per million (ppm) and cerium (Ce(IV)) at 1898 ppm. The high molarity of nitric acid effectively dissolves the calcined cake, ensuring the release of Th(IV) and Ce(IV) ions into the solution for further processing. Before its dissolution in nitric acid, the oxide cake derived from Monazite underwent thorough analysis using Inductively Coupled Plasma (ICP) and X-Ray Fluorescence (XRF) techniques. These analyses were essential for determining the composition of the cake, ensuring accurate quantification of its constituent elements (Table 1). Subsequently, the calcined cake was dissolute in 1 L of 8 mol HNO_3 (nitric acid), creating a nitrate stock solution. This solution was found to contain 2793 ppm of Th(IV) and 1898 ppm of Ce(IV).

Table 1 XRF and ICP-OES analysis of oxide cake, %

Element	XRF	ICP-OES
Th	3.6	3.9
Si	0	–
Ca	1.1	0.65
K	–	–
P	1.93	1.15
S	16.61	
V	–	–
Mn	–	–
Sc	–	0.001
Ce	24.8	21.3
La	6.4	5.7
Y	3.62	2.4
Sm	1.94	1.99
Nd	7.48	7.86
Pr	4.2	3.56
Gd	3.91	0.72
Eu	–	0.09
Nb	0.22	–
Dy	0.86	0.18
Ho	–	0.005
Tb	0.72	0.11
Yb	–	0.005
Er	–	0.25
Tm	0.23	–
Lu	0.012	0.0005

Batch adsorption experiments

This study investigated methods to adsorbing thorium (Th(IV)) and cerium (Ce(VI)) from a solution derived from monazite leaching (monazite leach liquor solution). The solution's acidity (pH) was adjusted using sodium hydroxide (NaOH) or nitric acid (HNO_3) to explore a range between 2 and 12. Initial Experimentations used for adsorbing these elements were a pH of 3, a contact time of 2 h, and room temperature.

To identify these optimal settings, a series of tests were conducted. In each experiment, 0.1 g of a specific material (PZMB) was added to 20 ml of the solution. The mixture was then shaken for 2 h at 200 rotations per minute using a magnetic stirrer. Four key factors were systematically investigated: pH (ranging from 1 to 6), temperature (ranging from 25 to 70 °C), the amount of PZMB added (ranging from 0.01 to 0.25 g), and the duration of contact (ranging from 5 to 120 min). It's important to note that during each experiment focused on a single factor, all other factors were maintained at constant values: pH of 3 (except when investigating pH), temperature of 25 °C (except when investigating temperature), 0.1 g of PZMB (except when investigating dosage), 20 ml of solution, and a contact time of 2 h (except when investigating contact time). By systematically varying these factors and analyzing the results, the most effective combination of conditions for removing Th(IV) and Ce(VI) from the monazite leach liquor solution was established.

After the adsorption experiments to adsorb Thorium (IV) and Cerium (VI) from the solution, the remaining concentrations were determined. The solutions were filtered using Whatman No. 41 filter paper to separate the PZMB adsorbent. The filtered solutions were then analyzed using a spectrophotometer and inductively coupled plasma optical emission spectrometry (ICP-OES) to quantify the remaining amounts of Th(IV) and Ce(VI). This analysis was crucial for understanding how effectively PZMB adsorbed these elements. Prior to the adsorption experiments, the initial concentrations of Th(IV) and Ce(VI) in the monazite leach liquor solution were measured using ICP-OES. The analysis revealed total Th(VI) and Ce(VI) concentrations of 2793 ppm and 1898 ppm, respectively. The adsorption capacity of PZMB for Th(IV) and Ce(VI) was calculated using the following equation:

$$q_e = \frac{\left(C_o - C_e\right) \times V}{m} \tag{2}$$

In this equation, C_o (mg/L) and C_e (mg/L) represent the initial and final concentrations of Th(IV) or Ce(VI), respectively. The term q_e (mg/g) represents the amount of Th(IV) or Ce(VI) adsorbed per gram of PZMB, m (g) denotes the mass of the PZMB adsorbent used, and V (L) is the volume of the untreated solution.

Renewal experiments

The experiments conducted to evaluate the renewal capabilities of PZMB involved adsorption–desorption cycles. In these experiments, 0.1 g of the new working compound PZMB was combined with a 20 mL monazite leach lacquer solution containing Th(IV) and Ce(VI), and stirred for 2 h at a temperature of 298 K. Post-adsorption, when the adsorbent was fully saturated with thorium and cerium, it was separated from the solution through filtration. The thorium and cerium-loaded adsorbent was then exposed to 20 mL of an eluent solution, heated to 298 K for 2 h to facilitate the desorption process. After the elution step, the sorbents were extensively washed with deionized water to eliminate any residual Th(IV) or Ce(VI), followed by overnight drying under vacuum at 50 °C, making them ready for supplementary sorption trials.

Results and discussion

Characterization

The chemical compositions of ZMB and PZMB were analyzed using (FT-IR). In the latter spectra, ZMB exhibited a

significant absorption peak at 3264 cm^{-1}, indicative of the intra-molecular hydrogen bonding among the four adjacent hydroxyl (OH) groups [24], as depicted in Fig. 1A. The absence of these specific absorption bands in the PZMB spectra implies that there was an interaction between phosphorus oxychloride and the phenolic oxygen atoms in the ZMB structure. This interaction suggests a modification in the chemical structure of ZMB upon treatment to form PZMB, highlighting the role of phosphorus oxychloride in altering the compound's molecular interactions and properties [25].

Aligned with prior research findings, the FTIR spectroscopic analysis of the PZMB Adsorbent's ligand reveals a prominent absorption peak at 1647 cm^{-1}, indicative of the azomethine group's υ (N=C) stretching vibration [26]. This feature suggests the presence of the azomethine (N=C) group within the compound. The spectrum also displays bands at 1517 and 1562 cm^{-1}, which are associated to the stretching vibrations of the pyridine ring's υ (C=N) groups [27], and additional bands at 1382 and 1456 cm^{-1}, associated with the pyridine ring's υ (C=C) stretching frequencies. Furthermore, the absorption bands at 3182 cm^{-1} and 2975 cm^{-1} correspond to the stretching vibrations of aromatic and aliphatic (C–H) bonds, respectively. These spectral details are depicted in Fig. 1B, which also includes a water absorption band at 3357 cm^{-1} [28]. The introduction of new absorption bands at 2355 cm^{-1}, 1173 cm^{-1}, and 992 cm^{-1}, post-phosphorylation, signifies the formation of P–H, P=O, and P–OH stretching vibrations, respectively, underscoring the chemical transformations that occur as a result of the reaction [29].

BET Surface Analysis

The porosity and specific surface area (SBET) of ZMB and PZMB were determined at 77K using the Brunauer–Emmett–Teller (BET) method. The nitrogen sorption/desorption isotherms for both ZMB and PZMB displayed minimal hysteresis, characteristic of Type IV isotherms Fig. 2, suggesting mesoporous structures for both materials. The SBET value for PZMB was notably higher, recorded at 196.24 m^2/g, compared to ZMB's surface area of 112.76 m^2/g. Additionally, the phosphorylation process resulted in an increased pore volume for PZMB, rising slightly from 0.227 cm^3/g for ZMB to 0.324 cm^3/g for PZMB, as indicated in Table 2. This data confirms the classification of ZMB and PZMB as mesoporous materials and

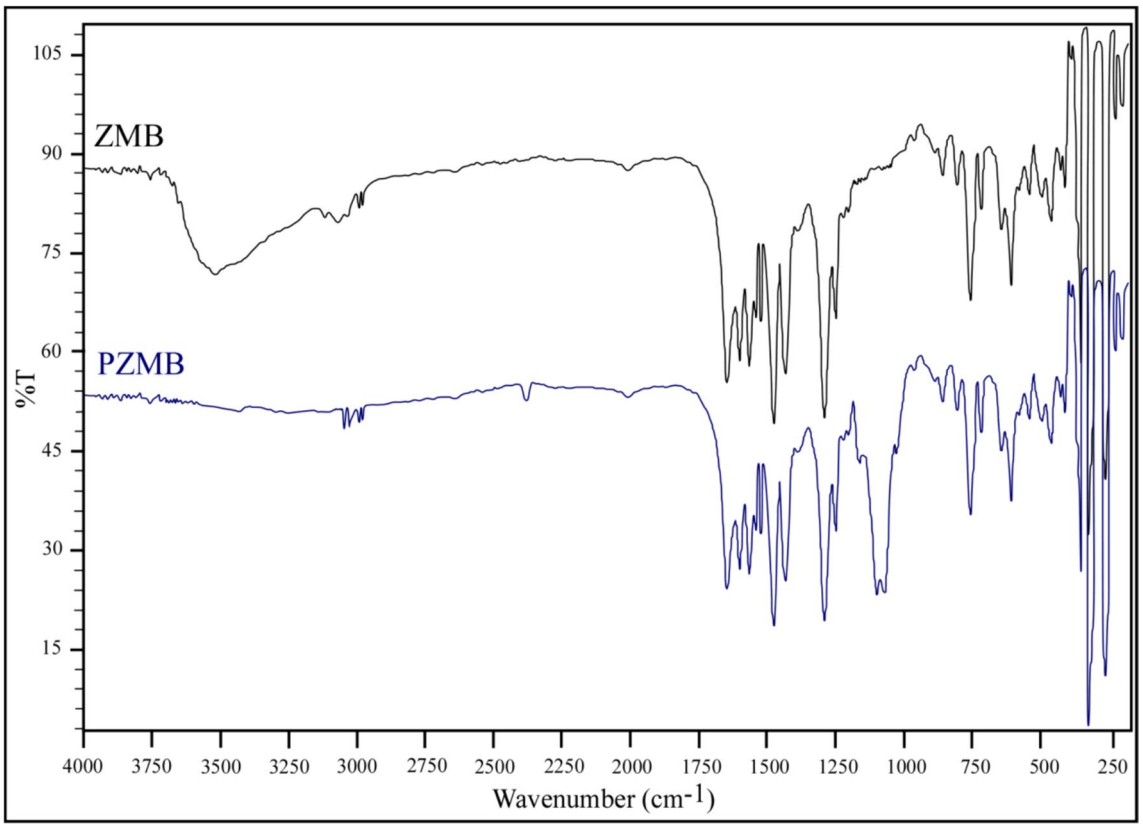


Fig. 1 FTIR spectrum of **A** ZMB, **B** PZMB

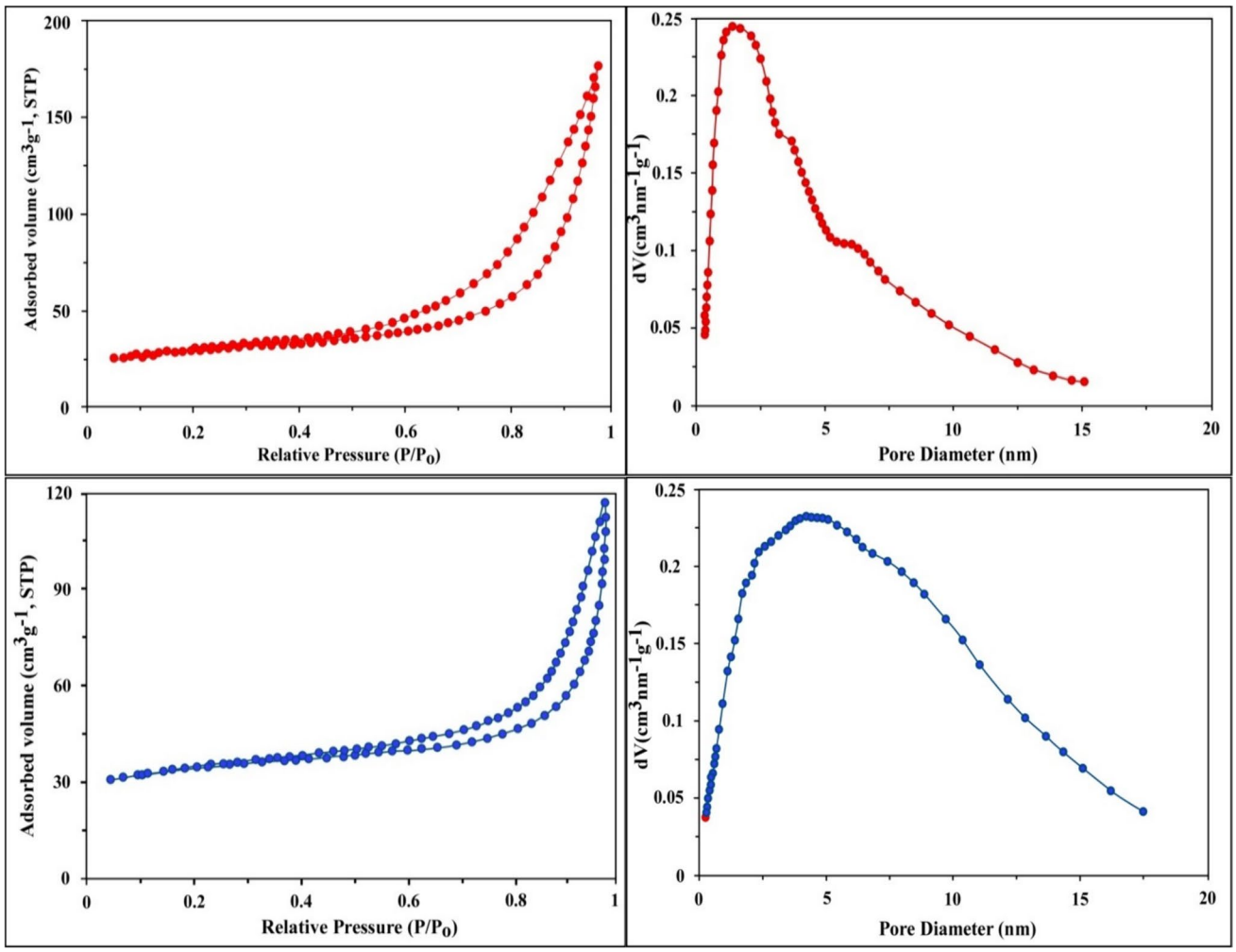


Fig. 2 **A**, **C** N2 sorption/desorption isotherms of ZMB and PZMB, and **B**, **D** pore volume distribution of ZMB and PZMB.3.3. 1H-NMR analysis

Table 2 ZMB and PZMB characteristics; Surface area and pore size

Adsorbant	BET surface area (m^2/g)	Total pore volume (cm^3/g)	Average pore diameter (nm)
ZMB	112.76	0.227	3.2
PZMB	196.24	0.324	1.98

highlights the impact of phosphorylation on enhancing the surface area and pore volume of PZMB.

^{1}H-NMR (400.06 MHz, DMSO-d_6, 25 °C, TMS) δ, ppm: 6.67 (m, $J = 3.21$ Hz, 4H, –PH group), 9.13 (d, $J = 3.21$ Hz, 4H, –OH group), 7.23–7.37 (d, 6H, –CH benzene ring), 7.11–8.42 (d, 3H, –CH of pyridine ring), 8.93 (s, 2H, –CH = N, imine group).

The ^{1}H-NMR spectral data is instrumental in identifying the positioning and environment of hydrogen atoms within the ligand's structure, offering insights into its molecular framework. This analysis, conducted with DMSO-d_6 as the diluent and at an operating frequency of 400 MHz, serves as an precious tool for clarifying the proton environment within the synthesized PZMB ligand, facilitating the structural prediction of the molecule. In this study, the protons attached to the benzene ring, denoted as –CH protons, are primarily assigned chemical shifts (δ) in the range of 7.23–7.37 ppm.

the variation in chemical shift assignments for the –CH protons of the benzene rings in the PZMB ligand is attributed to factors such as the orientation degree, proximity to, and distance from the ligand's active sites. These factors influence both the chemical shift values and the coupling constants observed. Additionally, the –CH protons of the pyridine ring exhibit chemical shifts similar to those of the benzene ring, suggesting comparable electronic environments. A notably high chemical shift value at $\delta = 8.93$ ppm for the –CH = N imine proton is observed, which is thought to be influenced by the degree

of electronegativity, as well as its proximity and distance from the nitrogen atom. This implies a considerable electronic interaction between the proton of the imine and the neighboring nitrogen atom.

The presence of a chemical shift at 6.67 ppm is associated with the protons of the phosphine group, which appear as a multiplet, indicating a complex environment around these protons. Furthermore, hydroxyl groups are characterized by a higher chemical shift, observed as a singlet at 9.13 ppm, indicating more deshielded protons due to their electronegative nature. The comprehensive characterization of the PZMB ligand using ^{1}H-NMR, as depicted in Fig. 3**,** provides a detailed insight into the molecular structure and the electronic environment of the various protons within the ligand, highlighting the utility of ^{1}H-NMR spectroscopy in elucidating structural details of complex molecules.

^{13}C-NMR analysis of PZMB

^{13}C-NMR (100.04 MHz, DMSO-d_6, 25 °C, TMS) δ, ppm: 111.56–113.01 (s, 6CH, benzene ring), 156.39 (s, 4C, benzene ring), 131.8–133.13 (s, 2C, benzene ring), 161.61 (s, 2CH, imine groups), 146.37–158.82 (s, 2C, pyridine ring), 119.32–144.2 (s, 3CH, pyridine ring).

^{13}C-NMR analysis with energy of 100.04 MH_Z and DMSO-d_6 as a diluent is an effective tool which gives significant information about quantity of carbon atoms in the synthesized PZMP ligand. It is obviously shown from the synthesized ligand that benzene ring has three main assignments. The first main assignment appeared around 111.56–113.01 ppm, which was related to the free 6 CH carbons in the two benzene rings. The second main assignment has a high chemical shift value at 156.39 ppm, which were related to four SP^3 hybridized carbon attached to the phosphine group (–OPO_2H_2). The third main assignment appeared around chemical shift value 131.8–133.13 ppm, which were related to two SP^3 hybridized carbon attached to the imine group (–CH=N). The higher chemical shift of 161.61 ppm is related to the two carbons of imine group. Also, it was found that pyridine ring in the synthesized ligand suffered from two main assignments at 146.37–158.82 ppm, which is related to the two carbon atoms attached to the imine group, and 119.32–144.2 ppm, which is associated to three –CH free carbon atoms. Description of the synthesized PZMB ligand using ^{13}C-NMR is illustrated in Figure SI. 1.

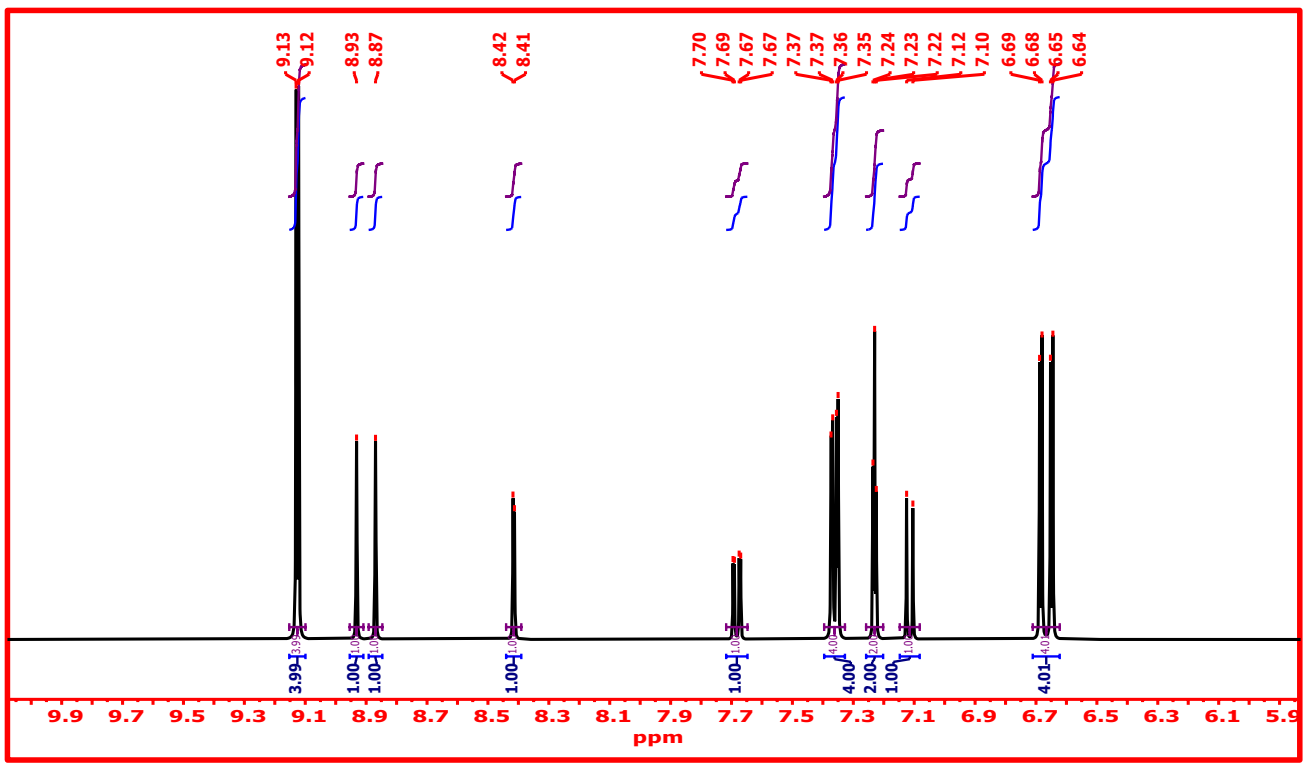


Fig. 3 1H-NMR analysis of PZMB

^{31}P-NMR analysis.

The ^{31}P-NMR analysis, conducted at 200.01 MHz using Chloroform-d as the solvent, effectively identifies the phosphorus component in the PZMP ligand, with a notable chemical shift at $\delta = 5.3$ ppm for the –PH group. This data, illustrated in Figure SI. 2, highlights the utility of ^{31}P-NMR in detailing the phosphorus atom's environment within the ligand.

GC–MS analysis of PZMB.

GC–MS (EI, 30 eV), m/z (% rel): [m/z]$^+$ of 605, 65, 138, 109, 17, 93, 266, 339, 496, 247 and 467. Anal. Calc. for $C_{19}H_{19}N_3O_{12}P_4$ (605.27 g/mol): C, 37.7; H, 3.16; O, 31.72; N, 6.94; P, 20.47. Found: C, 37.75; H, 3.15; O, 31.71; N, 6.9; P, 20.5.

GC–MS analysis is pivotal for predicting the chemical structure, identifying the most stable and abundant fragments (base peak), and assessing the purity of synthesized compounds. For the PZMP ligand, with a chemical formula of $C_{19}H_{19}N_3O_{12}P_4$, the radical cation ion peak at m/z = 605 with a 23% relative abundance (RA) confirms its molecular structure. This ligand exhibited several key fragmentation patterns: the phosphonic acid group $[H_2O_2P]^{\cdot}$ at m/z = 65 with associated of 13% (phosphonic acid group), para-dihydroxy benzaldehyde $[C_7H_6O_3]^{\cdot}$ at m/z = 138 with associated RA of 41%, and the base peak of diamino pyridine or dihydroxy benzene $[C_5H_7N_3]^{\cdot}$ at m/z = 99 with 99% relative abundance. Additionally, fragments such as ammonia gas $[NH_3]^{\cdot}$ at m/z = 17 with 26% RA, and amino pyridine $[C_5H_5N_2]_n$ with m/z = 93 and a RA of 51% (amino pyridine)., were observed, indicating a successful synthesis of the PZMB ligand. These findings underscore the efficacy of the synthesis process for the PZMB adsorbent, with a comprehensive description provided in Figure SI. 3, through GC–MS characterization.

Thermal stability and surface morphology of PZMB

The TGA curve for PZMB (Fig. SI. 4A) shows a mass loss at 25–121 °C due to the loss of surface water molecules. The second mass loss, observed at 122–237 °C, is attributed to the loss of coordinated water molecules or crystal lattice water molecules, as well as NH_3 [30]. The third mass loss, occurring between 238 and 500 °C, can be attributed to the evolution of the Schiff base ligand as CO and CO_2, resulting in carbonaceous waste. The final mass loss, observed between 500 and 700 °C, is due to the decomposition of the phosphonic acid group [31].

The surface morphological study: The surface morphology of Schiff base was studied by using scanning electron microscope (SEM). as shown in Fig. SI.4B&C.

The SEM of the PZMB material was irregular spherical grain structure while after the adsorption process its well dispersed, heterogeneous sized with highly agglomerated grains. Furthermore, the crystalline size of complexes was reduced when compared with ligand due to incorporation of metal ion [32–34].

Optimization of the factors affect the sorption of Th(IV) and Ce(VI) ions on the PZMB ligand.

Influence of pH

The importance of pH in the sorption of thorium and cerium is underscored by its effect on the active sites of the adsorbent's surface and the solubility of ions [35]. The study examined the adsorption efficiency at varying pH levels, with thorium and cerium concentrations in the solution reported as 2793 mg/L for Th(IV) and 1898 mg/L for Ce(IV), respectively. The investigation, spanning a pH range of 1–6, revealed that Th(IV) adsorption percentage increases with pH, peaking at an optimal pH of 3.5, as illustrated in Fig. 4a. Beyond this point, the rate of removal declines. The decrease in adsorption efficiency below a pH of 3 is attributed to competition with H^+ ions in the solution [36]. Conversely, an increase in pH beyond 3.5 leads to a reduction in clearance percentage due to the formation of complexes through hydrolysis precipitation [37].

The thorium uptake was observed to be decreased in the strongly acidic medium which may be due to the partial protonation of the PZMB binding sites and the competition with H_3O^+ in the solution [38]. Also the metals ions hydrolysis is suppressed by higher concentration of acid [39]. While with the pH increasing, the PZMB surface (+) charge decreases that reduces the columbic repulsion for the adsorbing Th(IV) ions. alternatively, with the pH increasing, over pH 4, the Th(IV) ions hydrolysis develops and along with monomeric species $[Th(OH)_3]^+$, $[Th(OH)_2]^{2+}$, and $[Th(OH)]^{3+}$ and polynuclear complexes for example $Th_2(OH)_2{}^{6+}$, $Th_4(OH)_8{}^{8+}$and $Th_3(OH)_5{}^{7+}$ are formed [40]. The Mononuclear Th(IV) species distribution in the aqueous solution is follows: at pH < 2.5, > 70% Th^{4+} and < 30% $Th(OH)^{3+}$, at value of pH 3, 35% Th^{4+} and 45% $Th(OH)^{3+}$ while at pH 4, 17% $Th(OH)^{3+}$, and 54% $Th(OH)_2{}^{2+}$ [41]. The predominant Th(IV) species that found at pH 3.5 at the adsorption process using PZMB are $Th(OH)^{3+}$ and $Th(OH)_2{}^{2+}$.

The peak adsorption of Th(IV) ions at around pH 3.5 can be attributed to their complexation with the phosphate and hydroxy groups present on the PZMB adsorbent surface. Beyond this pH value, the adsorption efficiency for Th(IV) ions reduces. This decrease in adsorption at higher

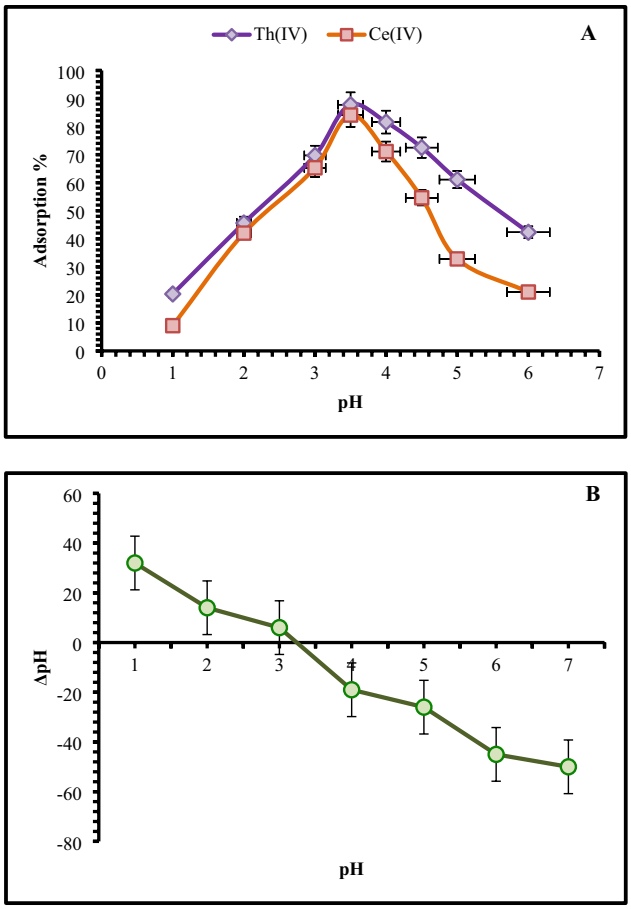


Fig. 4 **A** Effect of the solution pH on the adsorption% of Th(IV) & Ce(IV) using PZMB adsorbent. **B** pH point of zero charges of PZMB. [Th(IV) = 2793 mg/L & Ce(IV) = 1898 mg/L, 0.1 g PZMB, 20 mL solution, contact time = 30 min., room temperature]

pH levels is likely due to the formation of stable complexes such as$Th_3(OH)_5^{7+}$, $Th_4(OH)_8^{8+}$ and $Th_2(OH)_2^{6+}$ which may lead to damage on the PZMB adsorbent surface, as indicated by studies referenced in [42, 43].

The optimal pH level for the uptake of Ce(IV) ions onto the PZMB sorbent was identified to be 3.5, as depicted in Fig. 4a. The sorption capacity for Ce(IV) ions increased progressively from pH 1 to reach its maximum at pH 3.5. In highly acidic conditions, the prevalent forms of cerium are species like $[Ce(OH)]^{3+}$, $[CeO]^{2+}$ or $[Ce(OH)_2]^{2+}$ [44]. At such acidic pH levels, the adsorbent's surface binding sites undergo protonation, resulting in positively charged active groups. This leads to an increased electrostatic repulsion between the H^+ ions and Ce(IV) ions, diminishing the sorption efficiency due to the competitive interaction between H^+ and Ce(IV) for the available active sites on the sorbent's surface. As the pH value increases to 2 and above, the adsorbent surface begins to acquire a negative charge through the gradual deprotonation of its binding sites, improving the electrostatic attraction between the positively charged Ce(IV) ions and the adsorbent. This electrostatic attraction facilitates the sorption of Ce(IV) ions onto the PZMB surface under these conditions [45].

When the pH exceeded 4, there was a noticeable reduction in the sorption capacity for Ce(IV) ions, contrary to expectations of an increase. This reduction in adsorption efficiency can be attributed to the interactions between Ce(IV) ions and OH^- groups, leading to the formation of precipitates like $Ce(OH)_4$. The onset of cerium precipitation under these conditions begins to dominate the process, thereby reducing the amount of Ce(IV) ions available for adsorption onto the PZMB adsorbent [46].

For both Th(IV) and Ce(IV) ions, the point of zero charge (pH_{pzc}) of the PZMB adsorbent is illustrated in Fig. 4B, with the pH_{pzc} determined to be 3.27. At pH values exceeding this point, the surface of PZMB becomes negatively charged, $pH > pH_{pzc}$, which enhances its electrostatic attraction to the positively charged thorium and cerium species, facilitating their adsorption. Conversely, at lower pH levels (2.0–3.0), the adsorption capacity of PZMB for thorium is compromised due to the competitive presence of H^+ ions, which compete with thorium ions for the sorption sites [47]. As the pH raise beyond these levels, the competitive impact of H^+ reduces, leading to an improved adsorption capacity. The optimal adsorption of thorium on PZMB is achieved at a pH of 3.5, where the conditions are most favorable for overcoming the competition with H^+ ions and allowing for efficient adsorption of thorium ions onto the adsorptive.

Moreover, at low pH levels, the adsorption capability of PZMB for thorium is hindered by the protonation of its active sites. This protonation process leads to a reduction in the available binding sites for thorium ions, thereby diminishing the adsorbent's effectiveness [48]. However, at a pH of 3.5, there is a significant improvement in the deprotonation of the active sites on PZMB, which enhances the sorbent's capacity to uptake thorium. This shift towards deprotonation at the optimal pH level facilitates a more efficient interaction between thorium ions and the PZMB adsorbent, leading to improved adsorption efficiency [49].

Effect of contact time

In our investigation using PZMB, we carried out a series of time-dependent experiments at an optimal pH of 3.5, spanning contact times from 5 to 120 min. The sorption kinetics displayed in Figure SI. 5, reveal that within the first 60 min, the adsorption rates for thorium and cerium ions reached 98.8% and 94.2%, respectively, indicating that equilibrium for both systems was achieved after an hour. Extending the contact time beyond this point did not further enhance the adsorption efficiency for either ion type. The kinetic curves depicted in Fig. 8 illustrate two distinct phases of adsorption for Th(IV) and Ce(IV) onto PZMB. The initial phase shows

a rapid adsorption rate, attributed to the high concentration of ions in solution and the abundance of available active sites on the adsorbent's surface. The subsequent phase, approaching equilibrium, is characterized by a slowdown in intra-particle diffusion as the contact time extends, primarily because the concentration of adsorbate in the solution decreases and the external active sites on the sorbent become saturated. This saturation leads to a reduce in the rate of adsorption, eventually reaching a steady state. Therefore, according to these observations, a reaction time of 1 h was deemed optimal for all equilibrium experiments, ensuring efficient adsorption while maximizing the utilization of the adsorbent's capacity.

To analyze the rate constants of working metals adsorption on PZMB, Lagergren first-order rate.

illustration and pseudo-second-order rate illustration [50–52] (Eq. (3) and Eq. (4)) were used to suggest the kinetic adsorption data and understand the sorption process's dynamics. These models help in elucidating the rate at which adsorbate molecules interact with the adsorbent surface, as well as the potential mechanisms governing the sorption process

$$\log(q_e - q_t) = \log q_e - \frac{K_1 t}{2.303} \tag{3}$$

$$\frac{t}{q_t} = \frac{t}{q_e} + \frac{1}{k_2 q_e^2} \tag{4}$$

the process duration (t) is expressed in minutes, where k_1 represents the rate constant of adsorption (min^{-1}), q_t is the quantity of ions adsorbed at any given time (mg/g), and q_e is the amount adsorbed at equilibrium (mg/g). For first-order kinetics, which involve the rate constant k_1, the relationship between the adsorption capacity and time can be evaluated by plotting $\log(q_e–q_t)$ against time which gives a straight line. This approach, known as the Lagergren method, is visualized in Fig. 5A, B. However, it's noted that the adsorption processes for Th(IV) and Ce(IV) on some adsorbents do not align with the Lagergren first-order kinetic model. This discrepancy suggests that the adsorption behavior of these ions may involve more complex mechanisms or follow different kinetic orders.

Further analysis presented in Fig. 5C, D and detailed in Table 3 involves the calculated kinetic parameters and their respective regression coefficients (R^2). The pseudo second-order model, characterized by a higher R^2 value (0.9965) compared to the pseudo first-order model (0.9737), demonstrates a superior correlation with the experimental data. This significant distinction suggests that the adsorption kinetics of Th(IV) and Ce(IV) ions onto PZMB are more accurately represented by the pseudo second-order model, which implies that the adsorption process is predominantly governed by chemical adsorption involving the sharing or exchange of electrons between the ion species and PZMB [53, 54]. This conclusion indicates that the rate-limiting step in the adsorption of Th(IV) and Ce(IV) ions onto PZMB is better described by the mechanisms underlying the pseudo second-order adsorption model.

Impact of working adsorbent PZMB Dose

The influence of adsorbent dosage on the sorption efficiency of Th(IV) and Ce(IV) ions using PZMB is depicted in Fig. 6. The study varied the amount of sorbent used from 0.01 to 0.25 g while maintaining all other experimental conditions constant, starting with initial concentrations of 2793 mg/L for Th(IV) and 1898 mg/L for Ce(IV). The findings revealed that as the amount of PZMB increased, so did the surface area available for adsorption, which in turn enhanced the sorption of Th (IV) and Ce (IV) ions. A notable rise in sorption efficiency was detected as the dosage of the sorbent was improved from 0.01 to 0.15 g/L. Beyond this point, further increments in the adsorbent quantity did not significantly impact the rate of adsorption, indicating that the optimal adsorption efficiency for both Th (IV) and Ce (IV) ions was achieved at an adsorbent dosage of 0.15 g/L. This optimal dosage reflects the balance between the available surface area for adsorption and the concentration of the metal ions, representative the important role of sorbent dosage in maximizing sorption efficiency.

Adsorption isotherms

To investigate deeper into the mechanics of adsorption and to better understand the equilibrium behavior of adsorption processes, three isotherm models were employed: the Langmuir, Freundlich, and Dubinin–Radushkevich (D–R) models. Among these, the Langmuir isotherm model stands out due to its simplicity and its ability to closely match experimental data. The core assumption of the Langmuir model is that each adsorbent surface site possesses uniform energy for adsorption, permitting the attachment of only a single adsorbate molecule at each site [55]. According to this model, adsorption reaches a maximum capacity or equilibrium that corresponds to a complete monolayer of adsorbate on the adsorbent surface, beyond which sorption cannot proceed further. This saturation point is represented by a plateau in the Langmuir isotherm curve. Initially developed to describe adsorption in the gas phase, the Langmuir model has since been extensively applied to analyze equilibrium data for liquid-phase adsorption, providing valuable insights into the interactions between various solutes and adsorbents. This model's linear form allows for straightforward analysis and interpretation of adsorption phenomena. [56]. The linear form of the Langmuir isotherm model as follows [57]:

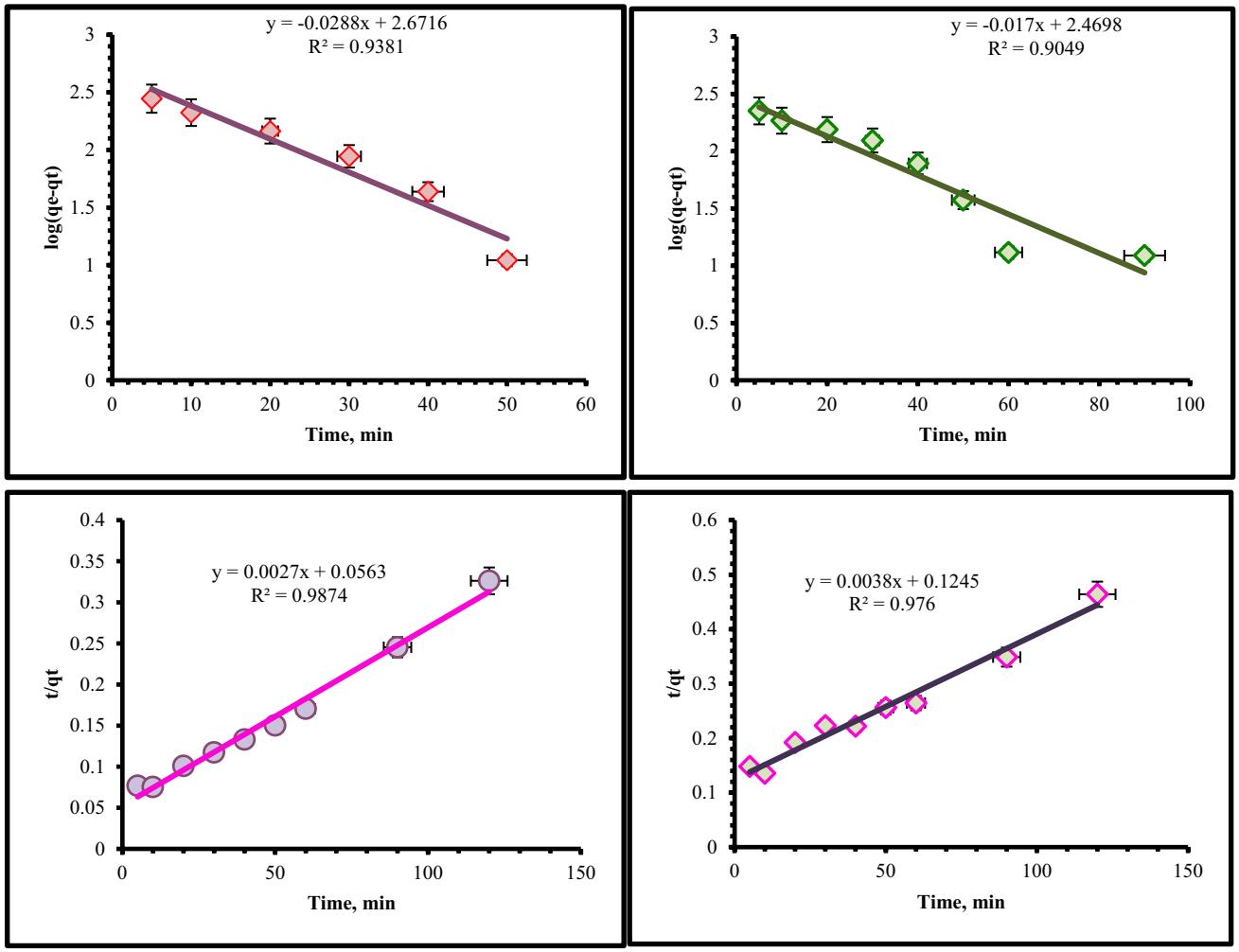


Fig. 5 **A** 1st (A) Th(IV) & (**B**) Ce(IV)—2nd (**C**) Th(IV) & (**D**) Ce(IV) order kinetics of Th(IV) and Ce(IV) ions adsorption upon PZMB. [Th(IV) = 2793 mg/L & Ce(IV) = 1898 mg/L, 0.1 g PZMB, 20 mL solution, contact time = 30 min., room temperature]

Table 3 Kinetic parameters of Th(IV) & Ce(IV) adsorption upon PZMB

Metal ions	1st ordered kinetic				2nd ordered kinetic		
	K_1	$q_{(max)cal}$	R^2	$q_{max(exp)}$	K_2	$q_{(max)cal}$	R^2
Th(IV)	0.0663	469.5	0.9381	367.9	0.00013	370.4	0.9874
Ce(IV)	0.0392	294.9	0.9049	246.5	0.00012	256.4	0.976

$$\frac{C_e}{q_e} = \frac{C_e}{q_m} + \frac{1}{q_m K_l} \quad (5)$$

where C_e represents the equilibrium concentration of metal ions in solution (mg/L), and q_e denotes the amount of Th(IV) and Ce(IV) adsorbed per gram of adsorbent (mg/g). The constants q_m and K_L within this model q_m indicating the maximum adsorption capacity (mg/g) and K_L reflecting the affinity or energy of adsorption (L/mg). These constants are derived from the linear relationship plotted between C_e/q_e and C_e, Fig. SI. 6, where the slope and intercept help determine q_m and K_L, respectively.

As the concentration of C_e increases, the adsorption system approaches saturation, meaning the surface of the adsorbent is fully occupied by adsorbate molecules up to its maximum capacity. Conversely, with a decrease in Ce concentration, the influence of the $K_L \cdot C_e$ is much less than one, aligning the Langmuir isotherm with Henry's Law, which applies to low concentrations of adsorbate. A key feature of the Langmuir model is the equilibrium parameter or the dimension-less constant separation factor (R_L), which

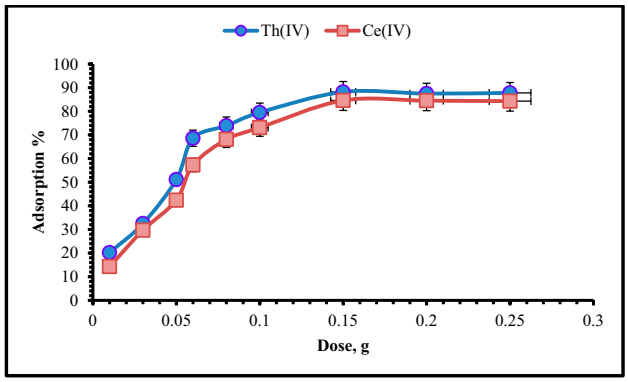


Fig. 6 Effect of PZMB dose on the adsorption efficiency of Th(IV) and Ce(III). [Th(IV) = 2793 mg/L & Ce(IV) = 1898 mg/L, 0.1 g PZMB, 20 mL solution, contact time = 60 min., room temperature]

provides insight into the feasibility of the adsorption process. This parameter is calculated using the equation [58]:

$$R_{\mathrm{L}} = \frac{1}{1 + K_{\mathrm{L}} C_{\mathrm{o}}} \tag{6}$$

where C_{o} is the initial concentration of the metal ions. The value of R_{L} indicates the nature of the adsorption process: $0 < R_{\mathrm{L}} < 1$ suggests favorable adsorption, $R_{\mathrm{L}} > 1$ indicates unfavorable adsorption, $R_{\mathrm{L}} = 1$ points to linear adsorption, and $R_{\mathrm{L}} = 0$ denotes irreversible adsorption. The data from the study reveals that for all evaluated conditions, the values of the dimensionless constant separation factor (R_L) are positive and less than one. This outcome underscores the highly favorable nature of the sorption process of PZMB for both Th(IV) and Ce(IV) metal ions, aligning with the principles of the Langmuir isotherm model.

The Freundlich adsorption model stands as the second model employed in this context. This approach is adept at explaining the adsorption dynamics within heterogeneous systems, which feature sites of varied binding energies. The Freundlich model offers a broader applicability, as outlined in the literature [59], the model's equation is presented in a linearized form as following:

$$\log q_{\mathrm{e}} = \log K_{\mathrm{f}} + \frac{1}{n} \log C_{\mathrm{e}} \tag{7}$$

The Freundlich constants, represented as n and K_{f} (expressed in mg/g), signify the system's heterogeneity level and the strength of adsorption affinity, respectively. By analyzing the linear relationship plotted between $\ln q_{\mathrm{e}}$ and $\ln C_{\mathrm{e}}$, it is probable to determine KF and n, corresponding to the plot's intercept and slope. A system exhibiting significant heterogeneity tends to surpass the linear isotherm boundaries when the value of n is sufficiently large. As the value of n increases beyond approximately 10, the behavior of the system approaches that of a non-reversible isotherm, indicating a move away from simple linear adsorption models.

$$\ln q_{\mathrm{e}} = \ln q_{\mathrm{D}} - B_{\mathrm{D}} (\varepsilon)^2 \tag{8}$$

Third adsorption isotherm model, known as the Dubinin–Radushkevich (D–R) model. This model assumes a diverse surface as its foundational premise. The D–R equation, when linearized, provides a framework for understanding adsorption on heterogeneous surfaces through its specific mathematical expression, as cited in [60].

$$E = \frac{1}{\sqrt{2B_D}} \tag{9}$$

It also aids in determining the adsorption process's nature and can be calculated using a designated equation Where q_{DR} (mmol/g) and B_{DR} ($\mathrm{mol^2/J^2}$) are the D–R isotherm constants related to the capacity and free energy of adsorption, and ε is the Polanyi potential that is equal to RT $\ln(1 + (1/C_{\mathrm{e}}))$. where R is the universal gas constant (8.314 J/mol·K), and T is the absolute temperature in Kelvin. and B_D, are linked to the adsorption capacity and the energy of adsorption E (in J/mol) for substances like Th(IV) and Ce(III) from the leach liquor to the surface of the adsorbent, in this case, PZMB. Through linear plotting of $\ln(q_{\mathrm{e}})$ versus ε^2, the D-R model parameters are calculated, as depicted in specified figures and tables (Figure SI. 6 and Table 4) [61, 62].

When the average adsorption energy E ranges from 1 to 8 kJ/mol, it is indicative of physical adsorption being the primary mechanism. On the other hand, when E falls between 8 and 16 kJ/mol, ion exchange is determined to be the leading process for adsorption. These differences are essential for discerning the specific adsorption mechanisms involved. The table referred to as Table 4 succinctly presents the controlling factor values for the models applied to both systems, indicating that the adsorption of Th(IV) and Ce(IV) by the PZMB adsorbent aligns well with the Langmuir isotherm model, as evidenced by R^2 values exceeding 0.989. According to data donated in Table 4, the calculated mean adsorption energy (E) for Th ions is 8.64 kJ/mol, and for Ce ions, it is 8.28 kJ/mol. These values indicate that the adsorption processes for both Th(IV) and Ce(IV) ions predominantly involve chemisorption, given that E exceeds the threshold of 8 kJ/mol typically associated with physical adsorption but falls within the range indicating chemisorption.Furthermore, the correlation coefficients (R^2) are 0.9594 for Th(IV) and 0.9639 for Ce(IV), demonstrating a strong fit to the Dubinin–Radushkevich (D–R) isotherm model. This strong correlation suggests that the D-R isotherm model accurately describes the adsorption behaviors of Th(IV) and Ce(IV) ions onto the PZMB adsorbent, reinforcing the model's applicability to chemisorption processes.

Table 4 Isotherms parameters of different models for sorption of Th(IV) and Ce(IV) ions by PZMB

Kinetic models	Parameters		
Langmuir isotherm	Equation	Th(IV)	Ce(IV)
		$y=0.0027x+0.0647$	$y=0.0041x+0.143$
	q_{max} (mg/g)	370.4	243.9
	K_1	0.0341	0.0287
	R^2	0.9762	0.9946
Freundlich isotherm	Equation	$y=0.363x+1.6185$	$y=0.4353x+1.3675$
	K_f (mg/g)	41.5	23.3
	$1/n$ (mg min/g)	0.363	0.435
	R^2	0.9273	0.9167
D–R isotherm	Equation	$y=-0.0067x+5.892$	$y=-0.0073x+5.5042$
	q_D (mg/g)	362.1	245.7
	B_D ($Mo1^2/KJ^2$)	0.0067	0.0083
	E_D(kJ/mo1)	8.64	8.28
	R^2	0.9594	0.9639
Practical capacity	q_{exp}	366.4	244.5

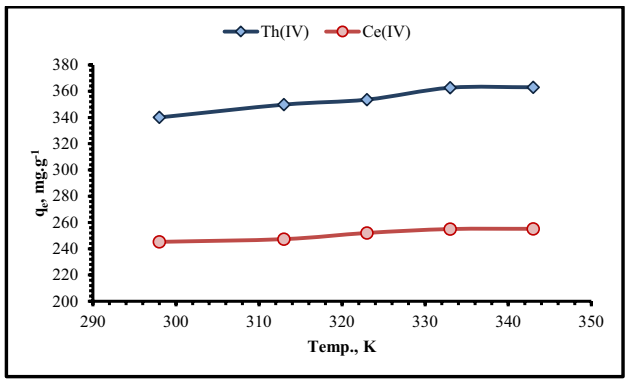


Fig. 7 The effect of temperature on the adsorption of Th(IV) and Ce(IV) on PZMB. [Th(IV) = 2793 mg/L & Ce(IV) = 1898 mg/L, 0.1 g PZMB, 20 mL solution, contact time = 60 min]

Effect of adsorption temperature (Adsorption thermodynamics)

When employing PZMB as an sorbent, the following effects of sample media temperature on the adsorption of Th(IV) and Ce(IV) ions were demonstrated. In a solution containing 2793 ppm Th(IV) and 1963 ppm Ce(IV) at a pH of 3.5, 0.15 g of PZMB was added at 298, 313, 323, 333, and 343 K. Figure 7 displays both the experimental and fitted data. Based on the data, it appears that the reaction rate grew little as the temperature rose. The data show that the uptake process is endothermic, meaning that the higher temperature is ideal for accelerating the reaction.

Table 5 displays the determined values for the thermodynamic factors governing the sorption process, specifically changes in enthalpy ($\Delta H°$), entropy ($\Delta S°$), and Gibbs free energy ($\Delta G°$). These values were derived from the equilibrium adsorption distribution and the variation in adsorption free energy, using the traditional Van't Hoff equation, as previously mentioned in sections (9, 10) and cited in references [46, 63, 64]. The evaluation of these thermodynamic parameters allows for the classification of adsorption processes into various types: spontaneous ($\Delta G° < 0$), indicating a process that occurs naturally without external energy input; non-spontaneous ($\Delta G° > 0$), requiring energy input to proceed; endothermic ($\Delta H° > 0$), absorbing heat from the surroundings; or exothermic ($\Delta H° < 0$), releasing heat. This classification aids in understanding the inherent nature and energy dynamics of the adsorption process.

$$\mathrm{Log}K_d = \frac{\Delta S}{2.303R} - \frac{\Delta H}{2.303RT} \tag{10}$$

$$\Delta G° = \Delta H° - T\Delta S° \tag{11}$$

where T represents the temperature of the adsorbing experiment (K), and R is the gas constant (8.314 J/(mol K)). the

Table 5 Thermodynamic factors for Th(IV) and Ce(IV) ions adsorption by PZMB at different temperatures

Metal ions	$\Delta H°$ (kJ mol^{-1})	$\Delta S°$ (J mol^{-1} K^{-1})	$\Delta G°$ (kJ mol^{-1})				
			298 K	313 K	323 K	333 K	343 K
Th(IV)	33.14	44.59	−13.25	−13.92	−14.37	−14.81	−15.26
Ce(IV)	30.87	42.38	−12.59	−13.24	−13.66	−14.08	−14.51

determination of ΔH and ΔS is simplified through the examination of the plot of log K_d versus $1/T$. Figure SI.7, illustrates this relationship, from which the slope and intercept can be extracted to compute ΔH and ΔS, respectively.

For Th(IV), the analysis yields a slope of − 1.731 and an intercept of 2.329 with a correlation coefficient (R^2) of 0.9669. For Ce(IV), the slope is − 1.612 and the intercept is 2.214, with an R^2 value of 0.9363 Figure SI.7. The negative slope in both cases correlates with a positive ΔH, signifying that the sorption processes for Th(IV) and Ce(IV) are endothermic. The temperature-dependent increase in negative $\Delta G°$ values suggests that adsorption becomes more favorable and energetically efficient at higher temperatures. This phenomenon could be attributed to the enhanced mobility of solute molecules at raised temperatures, facilitating their increased interaction and adsorption on the adsorbent surface [65]. Table 5

The positive values of $\Delta S°$ highlighted in the context suggest an rise in disorder and randomness at the solid-solution interface. This increase is attributed to the displacement of water molecules previously adsorbed on the surface of the adsorbent by metal cations—specifically Th(IV) and Ce(IV) ions—during the adsorption process. Table 5.

Desorption—regeneration studies

Cerium regeneration The investigation into the desorption of metal ions from a metal-loaded sorbent focused on evaluating the potential for both the reuse of the sorbent and the recovery of valuable metal ions, specifically Ce(IV). The process began with the exposure of the Ce(IV)-loaded PZMB adsorbent to aqueous solutions of reducing agents, aimed at selectively back-extracting Ce(IV) by reducing it to its trivalent state.

Following the successful back-extraction of Cerium in its trivalent form, the study proceeded to address the desorption of Thorium. The residual PZMB adsorbent, still loaded with Thorium, was then treated with various eluents to back-extract the Thorium ions. The efficiency of this process, referred to as stripping or elution efficiency, was quantitatively assessed by measuring the amount of M(IV) ions (in this context, Thorium) initially present in the adsorbent compared to the amount successfully removed.

The research placed significant emphasis on the efficiency of elution as well as the regeneration of the extractant. The findings highlighted the effectiveness of reducing Ce(IV) to Ce(III) as a strategic approach for enhancing the stripping process, due to the lower extraction efficiency of PZMB towards Ce(III), thereby facilitating its removal from the adsorbent. This approach not only aids in the recovery of valuable metals but also contributes to the sustainability of the adsorption–desorption process by enabling the reuse of the sorbent.

Stannous chloride ($SnCl_2$), sodium dithionate ($Na_2S_2O_6$), ascorbic acid ($C_6H_8O_6$), and hydrogen peroxide (H_2O_2) were employed as reducing agents to facilitate the selective removal of cerium. The experimental setup involved treating 1.5 g of PZMB loaded with Th(IV) and Ce(IV) ions, ensuring a contact time of 15 min, maintaining a temperature of 25 ± 2 °C, and using a 1 M concentration of the reducing agent. Figure 8A, illustrated the elution efficiencies of these eluents were compared, with sodium dithionate ($Na_2S_2O_6$), demonstrating superior performance in cerium recovery, likely due to its higher separation efficiency as indicated in the literature [66, 67].

Further experimentation focused on the effects of varying sodium dithionate concentrations on the recovery efficiency of Ce(III). By adjusting ($Na_2S_2O_6$) concentrations from 0.1 to 3 M, while keeping all other experimental conditions constant, it was observed that a concentration of 2 M ($Na_2S_2O_6$) enabled the recovery of 76.3% of the loaded Ce(IV), showcasing the impact of concentration on recovery efficiency Fig. 8B.

Additionally, the study explored the impact of elution time on the recovery process. By extending the duration from 1 to 60 min, it was found that a period of 50 min was optimal, achieving a near-complete recovery of Ce(III) from the loaded sorbent, with an efficiency of 99.4%. Figure 8C

To recover pure cerium, the eluting solution is boiled for 30 min and cooled to enable cerium precipitation. The solution's pH is adjusted to 1, and 5 g/L of EDTA is added to bind impurities. Ammonia is then introduced gradually, forming a cerium hydroxide precipitate. This precipitate is washed until the pH is neutral and dried at 100 °C. It's then calcined at 850 °C to produce cerium oxide, which is analyzed using XRD and EDX to confirm its purity. This method ensures the high-purity production of cerium oxide through controlled precipitation, washing, drying, and calcination. The crystallinity and purity of the cerium oxide product were assessed through X-ray diffraction analysis. The data indicated that the XRD pattern of the product aligns with that of CeO_2, as referenced in the JCPDS file 01-075-0390. This match confirms the successful synthesis of pure cerium oxide.

Thorium regeneration The regeneration ability of an adsorbent, crucial for assessing its practicality and feasibility, was examined for thorium-loaded PZMB using various eluting agents (H_2SO_4, EDTA, $NaNO_3$, HNO_3, and NaOH) at a concentration of 0.5 M. The results, displayed in Fig. 9A, indicate that HNO_3 was the most effective eluting agent. Further testing, shown in Fig. 9B, revealed that a 1 M concentration of HNO_3 was optimal for regenerating the adsorbed Th(IV) ions, with lower concentrations proving less effective. Additionally, Fig. 9C demonstrates that a 30-min contact time was ideal for thorium regeneration, significantly recovering

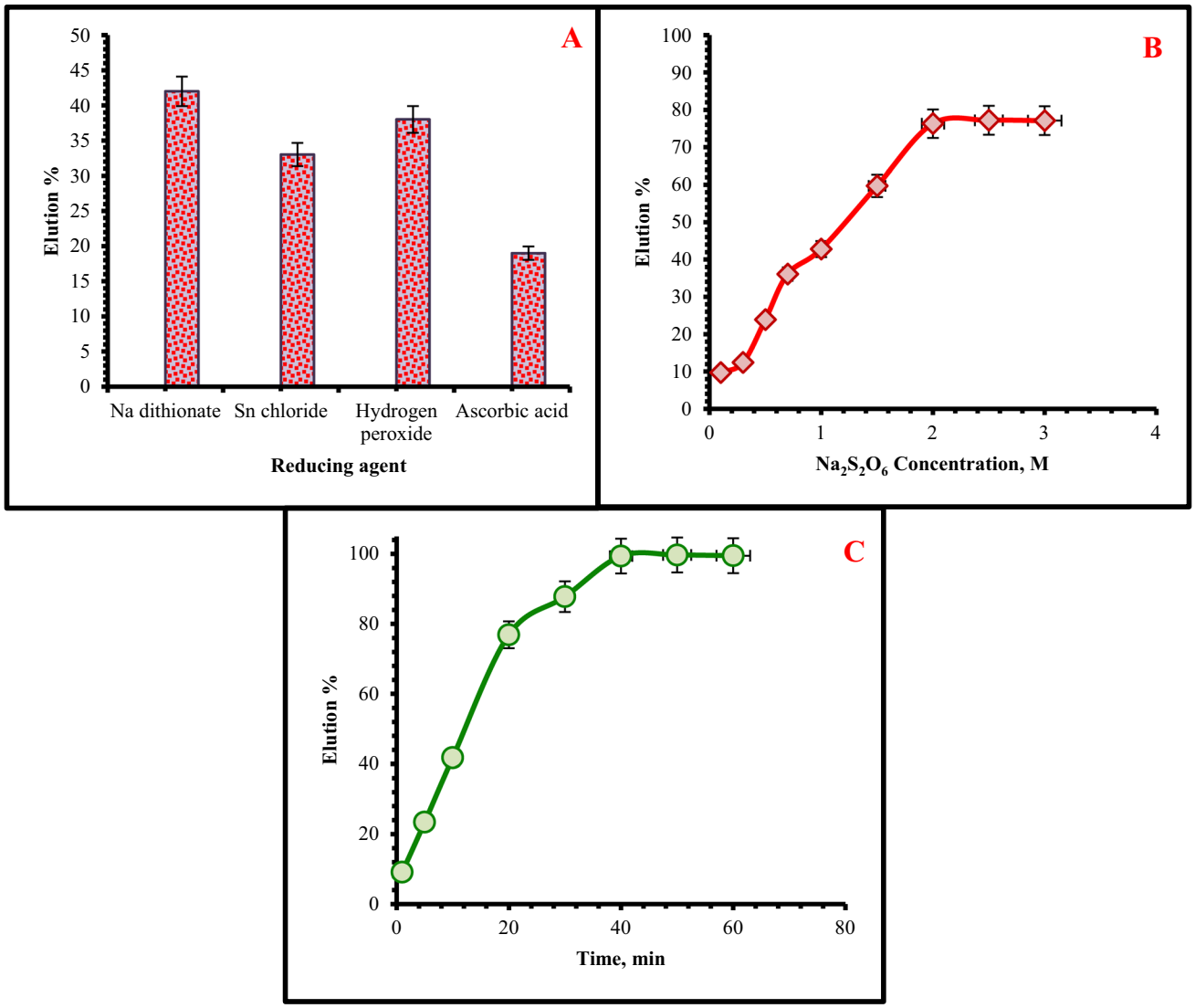


Fig. 8 **A** Elution of Cerium from PZMB surface by using different eluting solutions and **B** using different concentrations of HNO3 solution (**C**) at different elution times

the thorium content from PZMB across a timeframe of 5 to 90 min, highlighting the importance of both concentration and time in the regeneration process.

To obtain a pure thorium product, the recovered thorium underwent a precipitation process. Initially, the pH of the thorium solution was adjusted to value of 2 via 10% nitric acid (v:v). Subsequently, 30% hydrogen peroxide (v:v) was gradually added under continuous stirring as the solution was heated to 50 °C. The addition of ammonium hydroxide then increased the solution's pH to 3. The resultant precipitate was filtered and washed with distilled water. After drying, the thorium product was calcined at 700 °C for 2 h to achieve the final pure form. This process involves the reaction between $Th(NO_3)_4$ and H_2O_2, leading to the formation of thorium oxide as following equation

$$2Th(NO_3)_4 \cdot 4H_2O + 3H_2O_2 \rightarrow 7Th_2O_7 \cdot 4H_2O \downarrow + 8HNO_3 + 3H_2O \quad (12)$$

The $Th(NO_3)_4$ was then converted into $Th_2O_7{\cdot}4H_2O$ as the ending product [Eq. (12)]. The obtained product after calcination was confirmed by XRD and EDX analysis.

The XRD pattern of the final product is depicted in Fig. 10A, where all diffraction peaks match the cubic structure of ThO_2, as per JCPDS 42-1462. The absence of extraneous diffraction peaks confirms that the product is in a pure phase. The broadened peaks indicate the presence

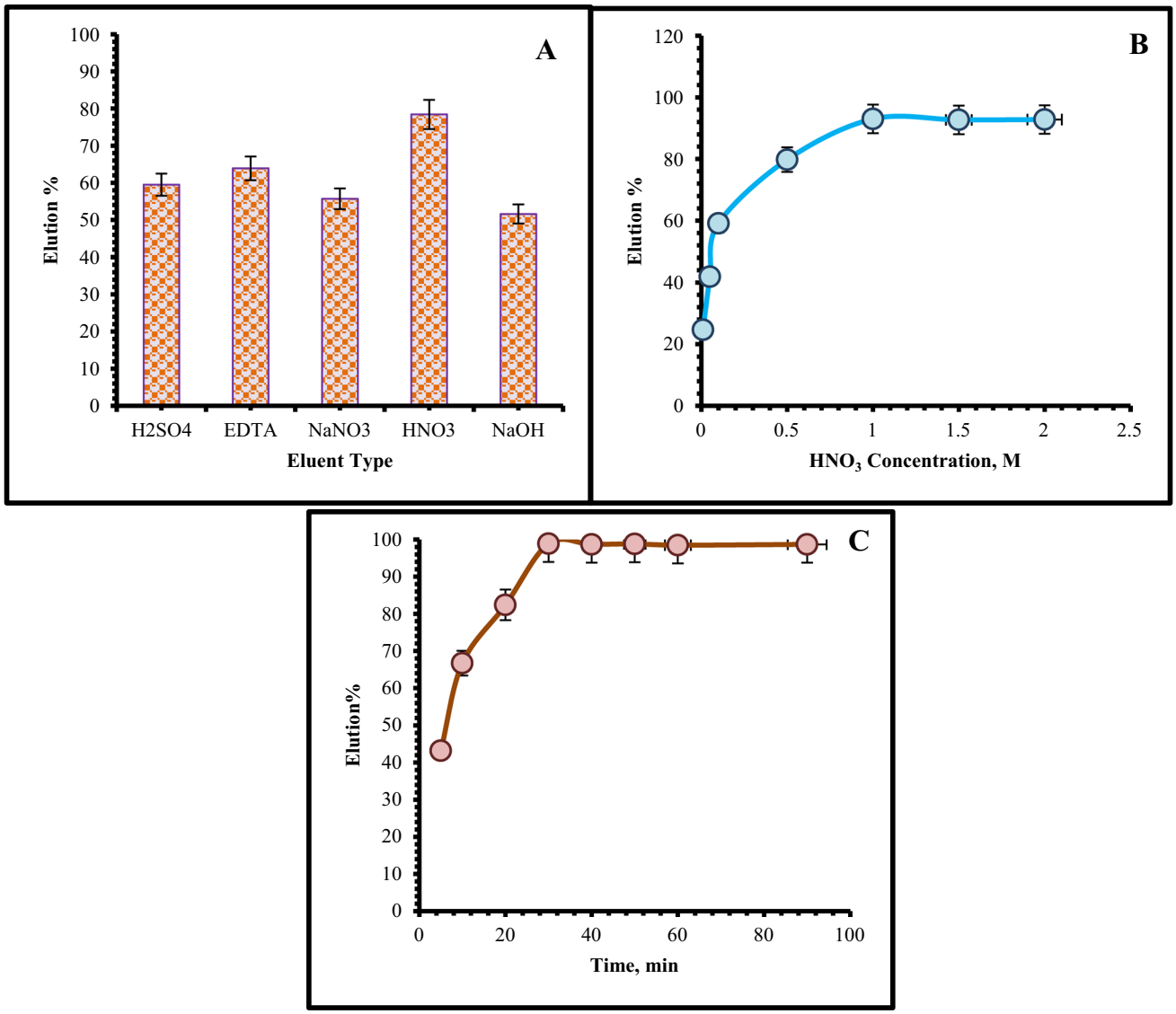


Fig. 9 **A** Elution of Th + 4 from PZMB surface by using different eluting solutions and **B** using different concentrations of HNO3 solution (**C**) at different elution times

of small ThO_2 nanoparticles, suggesting that the ThO_2 phase is not fully crystallized. The purity of thorium, free from any impurities, is further demonstrated in Fig. 10B through EDX analysis.

For the cerium product, the X-ray Diffraction (XRD) analysis, as shown in Fig. 10C, confirmed the purity of the CeO_2 product, with all peaks matching the conventional CeO_2 crystal structure as per JCPDS card No. 81-0792 [68]. The absence of additional diffraction peaks suggests the product is a pure phase. Also, an Energy Dispersive X-ray (EDX) study indicated the absence of contaminants within the cerium product, highlighting the no need for further purification or analysis to identify these impurities. Figure 10D.

Mechanism of the interaction between PZMB and Th(IV) and/or Ce(IV)

The findings indicate that PZMB exhibited a superior adsorption capacity maximum, likely due to the introduction of phosphate anions, which add more negative charges to the adsorbent's surface (specifically, two negative charges per phosphate anion), enhancing its affinity for thorium and cerium. The mechanism for thorium adsorption onto PZMB, as proposed in this study, is visually depicted in Fig. 11. The oxygen atoms in the phosphate anions within PZMB's structure facilitate a bridging interaction with Th(IV) and/or Ce(IV), where each phosphate anion contributes two negative charges on PZMB's surface. Consequently, a pair

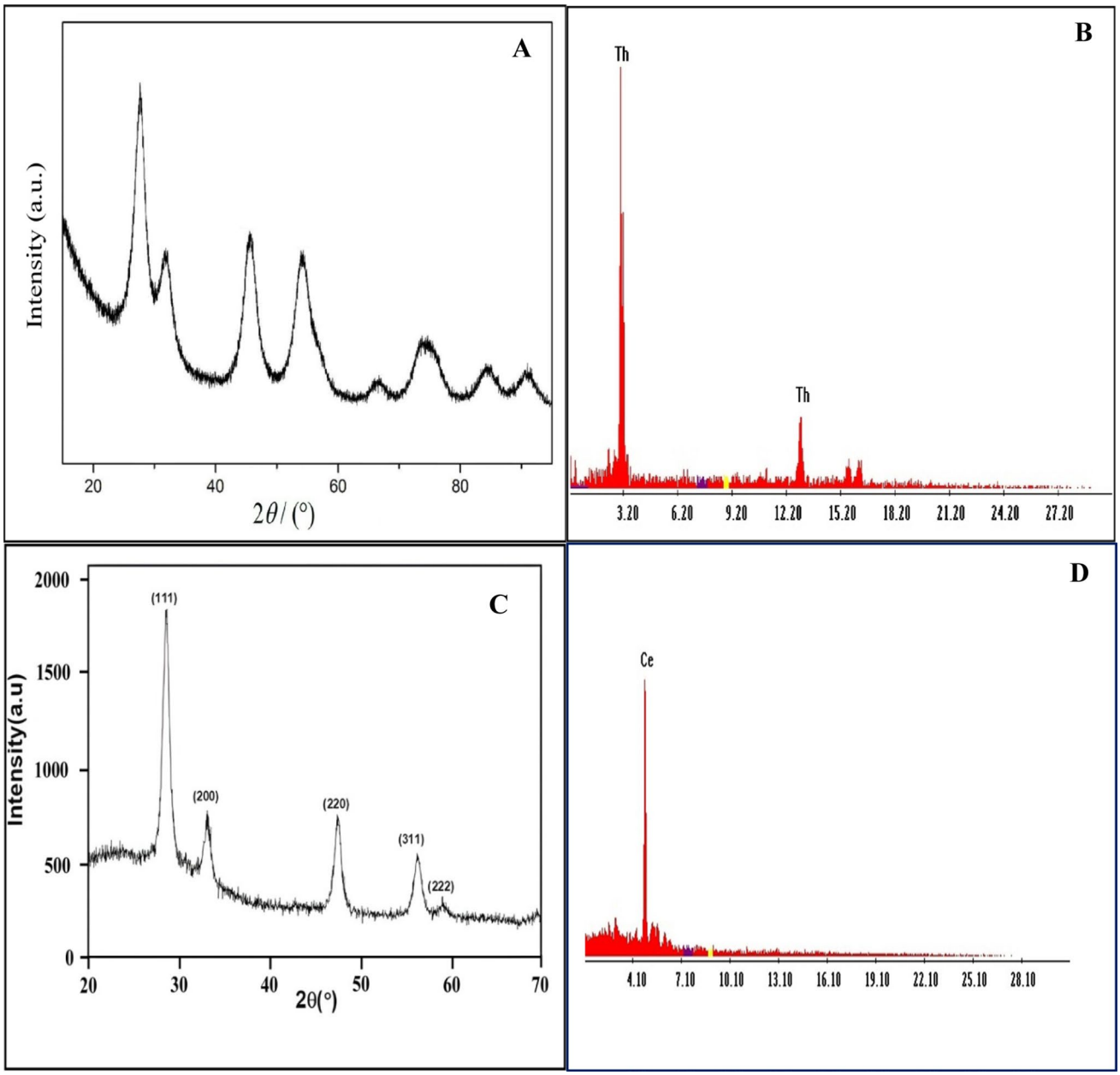


Fig. 10 **A** XRD images, and **B** EDX analysis of the obtained ThO2 product. **C** XRD images, and **D** EDX analysis of the obtained CeO2 product

of phosphate anions could potentially form a complex with thorium or cerium ions, as illustrated in Fig. 11.

The enhanced maximum adsorption capacity of PZMB is attributed to the incorporation of phosphate anions into the adsorbent, which significantly increases its surface negative charge, particularly beneficial for adsorbing positively charged thorium and cerium ions. Each phosphate anion contributes two negative charges, facilitating a stronger electrostatic attraction between the adsorbent and the metal ions. The schematic representation, as outlined in Fig. 11, illustrates the adsorption process, where the oxygen atoms in the phosphate groups on PZMB act as bridges, connecting the adsorbent to Th(IV) and/or Ce(IV) ions. [69] This interaction allows thorium and cerium ions to form complexes with two phosphate anions each, indicating a synergistic effect that improves the adsorption capacity of PZMB for these metal ions.

The adsorbent was analyzed using FTIR and EDX techniques before and after the adsorption process. The FTIR analysis after adsorption showed positive shifts in the stretching vibrations of P–H, P=O, and P–OH bonds from 2355 cm^{-1}, 1173 cm^{-1}, and 992 cm^{-1} to 2338 cm^{-1}, 1160 cm^{-1}, and 980 cm^{-1}, respectively. These shifts confirm the interaction between Th(IV) and Ce(IV) with the

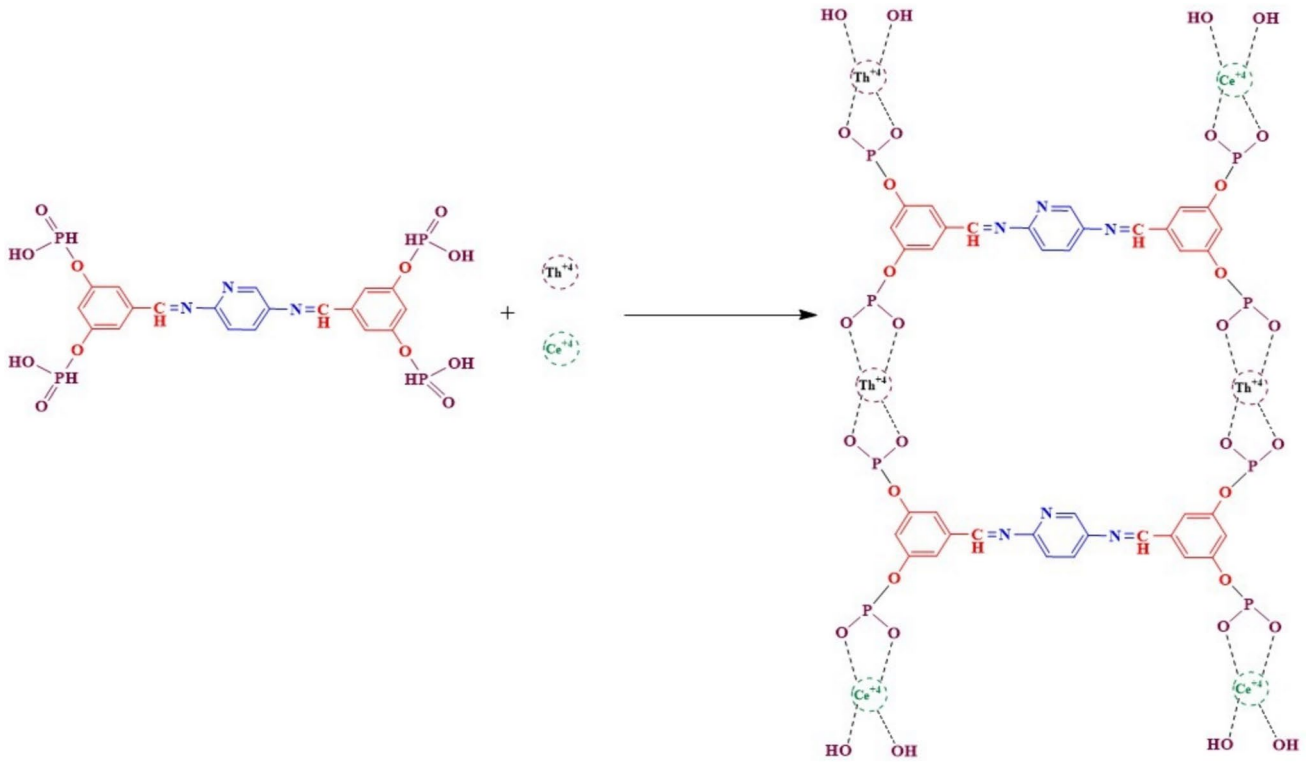


Fig. 11 Schematic diagram of the proposed mechanism of thorium and/or cerium adsorption onto PZMB

phosphonate functional group. Additionally, EDX analysis was performed for the PZMB adsorbent before and after adsorption process, and the results (Fig. 12B, C) show the appearance of Th(IV) and Ce(IV) peaks, further confirming the adsorption process using the PZMB adsorbent.

Recycling of the PZMB adsorbent

From Fig. 12D, The regeneration capability of the synthesized PZMB, a key factor in assessing an adsorbent's effectiveness and practicality, was explored through desorption experiments. Initially, PZMB loaded with cerium underwent desorption for 40 min using a 2 M $Na_2S_2O_6$ solution, followed by a desorption experiment on thorium-loaded PZMB for 30 min with a 1M HNO_3 solution. The ability of PZMB to regenerate was evaluated over seven adsorption–desorption cycles at 298 K. The findings revealed a gradual decrease in the adsorptive capacity of PZMB: from 369.79 mg g^{-1} it declined to 362.26 mg g^{-1} after three cycles, further reduced to 351.3 mg g^{-1} after five cycles, and ultimately dropped to 337.79 mg g^{-1} after seven cycles. This decrease in adsorption capacity over successive cycles was attributed to the loss of adsorbent mass and the depletion of non-renewable active sites.

Comparison between the studied adsorbent and the literature studied

The data presented in Tables 6 and 7 illustrate the superior performance of PZMB as an adsorbent for thorium (Th(IV)) and cerium (Ce(IV)) ions under varied experimental conditions. This comparison highlights PZMB's exceptional maximum sorption capacity for Th(IV) ions, surpassing that of other reported adsorbents. Furthermore, when it comes to the adsorption of Ce(IV), PZMB demonstrates a significantly higher capacity than that of other described adsorbents. This indicates the effectiveness of PZMB in binding and removing these specific metal ions from solutions, underscoring its potential utility in treating contaminated water or for use in purification processes where the removal of thorium and cerium is required.

Conclusion

In this research, PZMB was developed as an innovative Schiff base adsorbent, showing significant efficacy in removing thorium and cerium ions from monazite leach liquor solutions through adsorption. To ensure the successful synthesis of PZMB, it was subjected to an extensive series

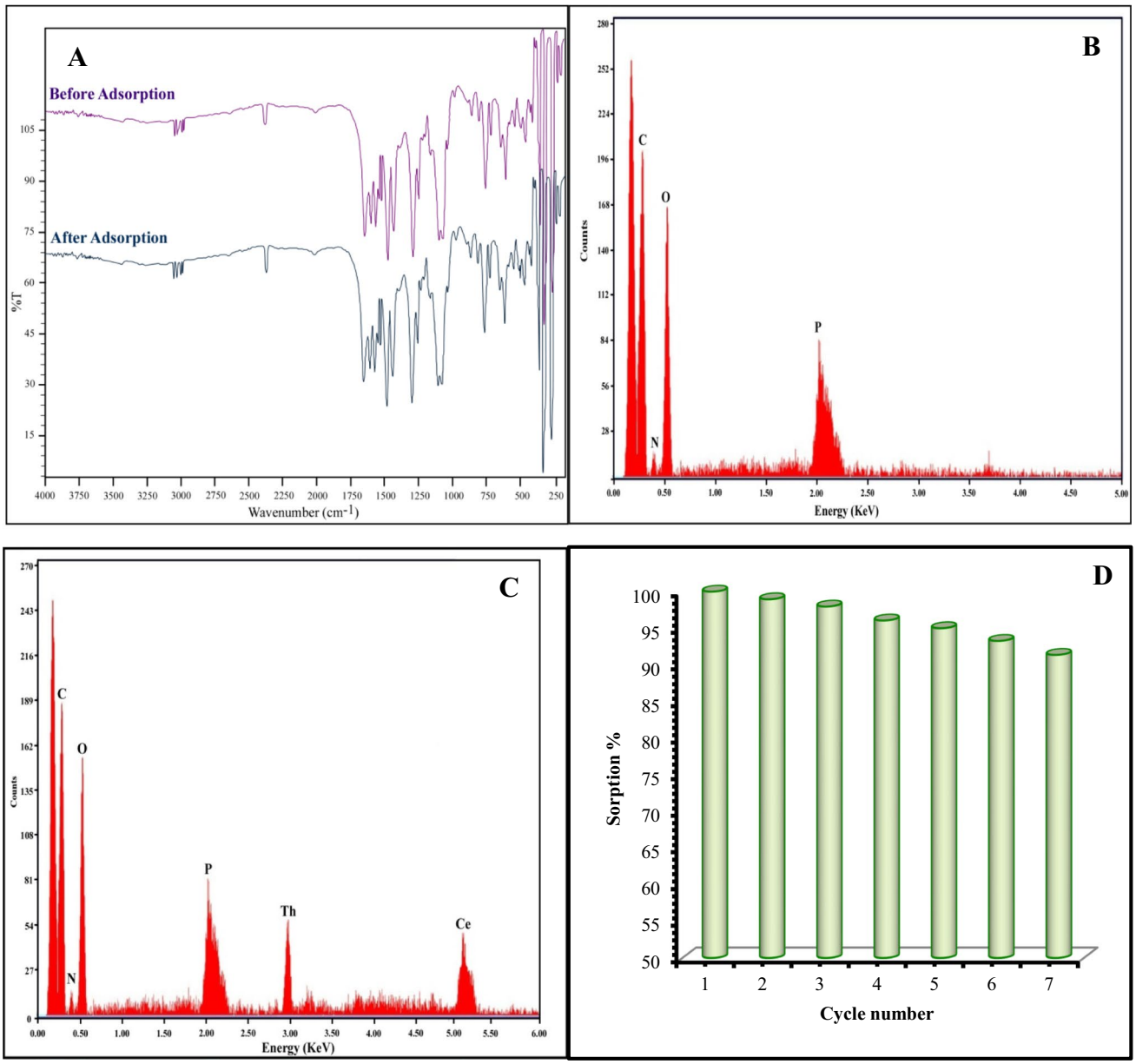


Fig. 12 **A** FTIR analysis of the PZMB adsorbent, **B** EDX analysis of PZMB adsorbent before adsorption process, **C** EDX analysis of PZMB adsorbent after adsorption process, and **D** Recycling of PZMB for the adsorption of Th(IV) and Ce(IV) ions

of characterization tests, including (FTIR, GC–MS, TGA, and NMR) studies. These analyses confirmed the structural integrity and functional properties of the synthesized sorbent.

Optimal parameters controlling the adsorption process were identified as a pH of 3.5 and a sorption duration of 60 min at ambient temperature, which were found to be crucial for maximizing the uptake of Th(IV) and Ce(IV) ions by PZMB. Furthermore, the adsorption mechanism was thoroughly investigated through kinetic and thermodynamic investigates, and the data were accurately modeled using the Langmuir and Dubinin–Radushkevich (D–R) isotherm models. The adsorption capacities achieved with PZMB were remarkable, reaching up to 346.4 mg/g for thorium and 244.53 mg/g for cerium, showcasing its potential as a highly efficient adsorbent for the elimination of these ions from their solution. The negative values of ΔG° across all temperature ranges confirm that the sorption of Th(IV) and Ce(IV) ions onto BZMP is spontaneous, with the process being endothermic as suggested by the positive ΔH°. This endothermic nature implies that the system absorbs heat during the adsorption process, which is conducive to the sorption of Th(IV) and Ce(IV) ions. Additionally, the positive ΔS° value indicates an rise in randomness at the

Table 6 Comparative study of the Th(IV) adsorption capabilities by PZMB with the different known adsorbents

Adsorbent	Capacity (mg/g)	References
BSP biomass adsorbent	125	[70]
graphite carbon nitride	108.18	[71]
Al Dope ZnO	192.3	[72]
Ion-imprinted chitosan resin	161.3	[73]
Silica beads	248.2	[74]
Magnetite nanoparticle	107.2	[75]
Amino naphthol sulphonate-chitosan	252.6	[76]
Mesoporous g-C_3N_4	196.1	[71]
Ion-imprinted chitosan	325	[77]
Amino group-functionalized titanosilicate	83.4	[78]
PZMP	346.4	This study

solid-solution interface, suggesting that the adsorption activities lead to a more disordered distribution of adsorbed species.The treatment of monazite leach liquor solution with BZMP successfully facilitated the sorption of Th(IV) and Ce(IV) ions, allowing for their subsequent precipitation. The characterization of the precipitated thorium and cerium oxides through (XRD) and (EDX) analysis confirmed their composition, further verifying the effectiveness of BZMP as an adsorbent for the purification of solutions containing these ions.

Table 7 Comparative study of the Ce(IV) adsorption capabilities by PZMB with the different known adsorbents

Adsorbent	Capacity (mg/g)	References
Prawn carapace particles	218.3	[79]
Diglycolic acid functionalized electrospun polystyrene nanofiber (PS-DGAnf)	152.5	[80]
chromium-based metal–organic framework functionalized with N- (phosphonomethyl) iminodiacetic acid)	49.0	[81]
Poly (acrylic acid) brushes-decorated attapulgite	295.4	[82]
Poly(allylamine)/silica composite	111.8	[83]
Ligand immobilized nano-composite	150.37	[84]
Turbinaria conoides	152.8	[85]
sulfosuccinic acid/polyvinyl alcohol/polyamide	142.11	[86]
Zn/Al Layered double hydroxide intercalated cellulose nanocomposite	96.25	[87]
Modified SBA-15 mesoporous silica	154.86	[88]
PZMB	244.53	This study

Supplementary Information The online version contains supplementary material available at https://doi.org/10.1007/s10967-024-09667-4.

Funding Open access funding provided by The Science, Technology & Innovation Funding Authority (STDF) in cooperation with The Egyptian Knowledge Bank (EKB).

Declarations

Conflict of interest The authors declare that they have no known competing financial interests or personal relationships that could have appeared to influence the work reported in this paper.

Open Access This article is licensed under a Creative Commons Attribution 4.0 International License, which permits use, sharing, adaptation, distribution and reproduction in any medium or format, as long as you give appropriate credit to the original author(s) and the source, provide a link to the Creative Commons licence, and indicate if changes were made. The images or other third party material in this article are included in the article's Creative Commons licence, unless indicated otherwise in a credit line to the material. If material is not included in the article's Creative Commons licence and your intended use is not permitted by statutory regulation or exceeds the permitted use, you will need to obtain permission directly from the copyright holder. To view a copy of this licence, visit http://creativecommons.org/licenses/by/4.0/.

References

1. Lankapati HM, Dankhara PM, Lathiya DR, Shah B, Chudasama UV, Choudhary L, Maheria KC (2021) Removal of lanthanum, cerium, and thorium metal ions from aqueous solution using ZrT hybrid ion exchanger. Sustain Energy Technol Assess 47:101415. https://doi.org/10.1016/j.seta.2021.101415
2. de Carvalho Gomes R, Yokoyama L, Marrero Vera Y (2021) Study of lanthanum-didymium separation by solvent extraction from a liquor conditioned with lactic acid. Miner Eng 170:107021. https://doi.org/10.1016/j.mineng.2021.107021
3. Ault T, Krahn S, Worrall A, Croff A (2018) Applications for thorium in multistage fuel cycles with heavy water reactors. Nucl Technol 204(1):41–58. https://doi.org/10.1080/00295450.2018.1468702
4. Du M, Peretz F, Boll RA, Mirzadeh S (2003) Thorium-229 for medical applications. ACS Symp Ser 868:193–204. https://doi.org/10.1021/bk-2004-0868.ch013
5. Zou D, Chen J, Li D (2014) Separation chemistry and clean technique of cerium(IV): a review. J Rare Earths 32(8):681–685. https://doi.org/10.1016/s1002-0721(14)60125-3
6. Chung KW, Yoon HS, Kim CJ, Lee JY, Jyothi RK (2020) Solvent extraction, separation and recovery of thorium from Korean monazite leach liquors for nuclear industry applications. J Ind Eng Chem 83:72–80. https://doi.org/10.1016/j.jiec.2019.11.014
7. Ramasamy DL, Puhakka V, Iftekhar S, Wojtuś A, Repo E, Ben Hammouda S, Iakovleva E, Sillanpaa M (2018) N- and O-ligand doped mesoporous silica-chitosan hybrid beads for the efficient, sustainable and selective recovery of rare earth elements (REE) from acid mine drainage (AMD): understanding the significance of physical modification and conditioning of the polymer. J Hazard Mater 348:84–91. https://doi.org/10.1016/j.jhazmat.2018.01.030
8. Wang F, Wang W, Zhu Y, Wang A (2017) Evaluation of Ce(III) and Gd(III) adsorption from aqueous solution using CTS-g-(AA-co-SS)/ISC hybrid hydrogel adsorbent. J Rare Earths 35:697–708. https://doi.org/10.1016/S1002-0721(17)60966-9

9. Zhang J, Zhong A, Huang G, Yang M, Li D, Teng M, Han D (2020) Enhanced efficiency with CDCA co-adsorption for dye-sensitized solar cells based on metallosalophen complexes. Sol Energy 209:316–324. https://doi.org/10.1016/j.solener.2020.08.096
10. Zhen J, Wang Z, Ni B, Ismail S, El-Baz A, Cui Z, Ni S (2024) Synergistic integration of Anammox and endogenous denitrification processes for the simultaneous carbon, nitrogen, and phosphorus removal. Environ Sci Technol 58(24):10632–10643. https://doi.org/10.1021/acs.est.4c00558
11. Tofan L, Bojoaga C-N, Paduraru C (2022) Biosorption for the recovery and analysis of rare earth elements and platinum group metals from real samples: a review. Environ Chem Lett 20:1225–1248. https://doi.org/10.1007/s10311-021-01330-8
12. Humelnicu D, Pui A, Malutan C, Malutan T, Humelnicu I (2020) Synthesis, characterization, and theoretical investigations of new uranium (VI) and thorium (IV) complexes with 1-furfurylaldehyde-derived Schiff bases as ligands. J Saudi Chem Soc 24(6):451–560. https://doi.org/10.1016/j.jscs.2020.04.001
13. Agnihotri S, Arora K (2010) Physicochemical investigations of Th(IV) and UO2(VI) complexes with new Schiff bases along with their toxic effects. Chem Sci Trans 7:1045–1054. https://doi.org/10.1155/2010/859034
14. Liu T, Duan G, Zeng Z (2009) Synthesis and characterization of cerium, thorium, and uranyl complexes with (E)-4-(4-methoxyphenoxy)-4-oxobut-2-enoic acid. J Coord Chem 62(13):2203–2211. https://doi.org/10.1080/00958970902769799
15. Li X, Fan G (2024) On strain localization of aeolian sand in true triaxial apparatus. Acta Geotech 19(5):3115–3128. https://doi.org/10.1007/s11440-024-02273-4
16. Cegłowski M, Schroeder G (2015) Preparation of porous resin with Schiff base chelating groups for removal of heavy metal ions from aqueous solutions. Chem Eng J 263:402–411
17. Zhang X, Jiao C, Wang J, Liu Q, Li R, Yang P, Zhang M (2012) Removal of uranium(VI) from aqueous solutions by magnetic Schiff base: kinetic and thermodynamic investigation. Chem Eng J 198–199:412–419
18. Tashkhourian J, Moradi Abdoluosofi L, Pakniat M, Montazerozohori M (2011) Sodium dodecyl sulfate coated alumina modified with a new Schiff's base as a uranyl ion selective adsorbent. J Hazard Mater 187:75–81
19. Dolatyari L, Yaftian MR, Rostamnia S (2016) Removal of uranium(VI) ions from aqueous solutions using Schiff base functionalized SBA-15 mesoporous silica materials. J Environ Manag 169:8–17
20. Wang J, Wang Y, Xu Lu, Wu Q, Wang Qi, Kong W, Liang J, Yao J, Zhang Ji (2017) Synthesis and structural features of phosphorylated Artemisia sphaerocephala polysaccharide. Carbohydr Polym 181:19–26. https://doi.org/10.1016/j.carbpol.2017.10.049
21. Huang P, Bi X, Gao J, Sun L, Wang S, Chen S, Fan X, You Z, Wang Y (2016) Phosphorylated poly(sebacoyl diglyceride)—a phosphate functionalized biodegradable polymer for bone tissue engineering. J Mater Chem B 4:2090–2101. https://doi.org/10.1039/C5TB02542G
22. Ibrahium HA, Awwad NS, Gado MA et al (2022) Physico-chemical aspects on uranium and molybdenum extraction from aqueous solution by synthesized phosphinimine derivative chelating agent. J Inorg Organomet Polym 32:3658. https://doi.org/10.1007/s10904-022-02421-x
23. Ali AH (2017) Coextraction and successive selective stripping of cerium(IV) and thorium from monazite leach solutions with tributyl phosphate (TBP). Radiochem 59:579–586. https://doi.org/10.1134/S10663622170600054
24. Cai Y, Wu C, Liu Z, Zhang L, Chen L, Wang J, Wang S (2017) Fabrication of a phosphorylated graphene oxide–chitosan composite for highly effective and selective capture of U(VI). Environ Sci Nano 4:1876–1886. https://doi.org/10.1039/c7en00412e
25. Mostafa KH, Eman IH, Gehad MG, Ehab ZM, Ahmed B (2012) Synthesis and characterization of a novel Schiff base metal complexes and their application in determination of iron in different types of natural water. Open J Inorg Chem. https://doi.org/10.1155/2012/859034
26. Al-Mohammadi NA-HA, Al-Fahdawi AS, Al-Janabi SS (2021) Design and characterization of new dinuclear macrocyclic dithiocarbamate complexes by the preparation of a free ligand derived from isopropylamine. Iraqi J Sci 62(1):1–15. https://doi.org/10.24996/ijs.2021.62.1.1
27. Buldurun K, Özdemir M (2020) Ruthenium(II) complexes with pyridine-based Schiff base ligands: synthesis, structural characterization and catalytic hydrogenation of ketones. J Mol Struct 1202:127266. https://doi.org/10.1016/j.molstruc.2020.127266
28. Abdel-Monem YK, Abouel-Enein SA, Safa M (2018) Synthesis, characterization and molecular modeling of some transition metal complexes of Schiff base derived from 5-aminouracil and 2-benzoyl pyridine. J Mol Struct 1152:115–127. https://doi.org/10.1016/j.molstruc.2017.12.005
29. Elbshary RE, Gouda AA, El Sheikh R, Alqahtani MS, Hanfi MY, Atia BM, Gado MA (2023) Recovery of W(VI) from wolframite ore using new synthetic Schiff base derivative. Int J Mol Sci. https://doi.org/10.3390/ijms24087423
30. Bajaber MA, Ragab HA, Sakr AK, Atia BM, Fathy WM, Gado MA (2022) Application of a new derivative of triazole Schiff base on chromium recovery from its wastewater. Sep Sci Technol 58(4):737–758. https://doi.org/10.1080/01496395.2022.2147440
31. Athod D, Vijay M, Islam N, Kannan R, Kharul U, Kurungot S, Pillai V (2009) Design of an "All Solid-State" supercapacitor based on phosphoric acid doped polybenzimidazole (PBI) electrolyte. J Appl Electrochem 39(7):1097–1103. https://doi.org/10.1007/s10800-008-9764-3
32. Sun X, Li R, Sun H, Olin PH, Santosh M, Fu B, Deng J (2024) Genesis of Pb–Zn-Ag-Sb mineralization in the Tethys Himalaya, China: early magmatic-hydrothermal Pb–Zn(-Ag) mineralization overprinted by Sb-rich fluids. Mineral Depos. https://doi.org/10.1007/s00126-024-01264-5
33. Raman N, Jeyamurugan R, Sudharsan S, Karuppasamy K, Mitu L (2013) Metal based pharmacologically active agents: Synthesis, structural elucidation, DNA interaction, in vitro antimicrobial and in vitro cytotoxic screening of copper(II) and zinc(II) complexes derived from amino acid based pyrazolone derivatives. Arab J Chem 6:235–247. https://doi.org/10.1016/j.arabjc.2012.04.010
34. Solomon EI, Hare JW, Gray HB (1976) Spectroscopic studies and a structural model for blue copper centers in proteins. Proc Natl Acad Sci USA 73(5):1389–1393. https://doi.org/10.1073/pnas.73.5.1389
35. Aydın H, Bulut Y (2008) Removal of copper(II) from aqueous solution by adsorption onto low-cost adsorbents. J Environ Manag 87(1):37–45. https://doi.org/10.1016/j.jenvman.2007.01.005
36. Mahmoud MA, Abutaleb A, Maafa IMH, Qudsieh IY, Elshehy EA (2019) Synthesis of polyvinylpyrrolidone magnetic activated carbon for removal of Th(IV) from aqueous solution. Environ Nanotechnol Monit Manag 11:100191. https://doi.org/10.1016/j.enmm.2018.10.006
37. Aksu Z (2002) Determination of the equilibrium, kinetic and thermodynamic parameters of the batch biosorption of nickel(II) ions onto Chlorella vulgaris. Process Biochem 38(1):89–99. https://doi.org/10.1016/S0032-9592(02)00051-1
38. Gado MA, Morsy AMA (2017) Thorium adsorption from waste effluents by phosphate-enhanced chitin. Radiochem 59:500–506. https://doi.org/10.1134/S1066362217050101

39. Li Z, He M, Li B, Wen X, Zhou J, Cheng Y, Zhang N, Deng L (2024) Multi-isotopic composition (Li and B isotopes) and hydrochemistry characterization of the Lakko Co Li-rich salt lake in Tibet, China: origin and hydrological processes. J Hydrol 630:130714. https://doi.org/10.1016/j.jhydrol.2024.130714
40. Hamza M, Wei Y, Khalafalla M, Abed N, Fouda A, Elwakeel K, Guibal E, Hamad N (2022) U(VI) and Th(IV) recovery using silica beads functionalized with urea or thiourea-based polymers—application to ore leachate. Sci Total Environ 821:153184. https://doi.org/10.1016/j.scitotenv.2022.153184
41. Li S, Wang L, Peng J, Zhai M, Shi W (2019) Efficient thorium(IV) removal by two-dimensional Ti_2CTx MXene from aqueous solution. Chem Eng J 366:192–199. https://doi.org/10.1016/j.cej.2019.02.056
42. Abbasizadeh S, Keshtkar AR, Mousavian MA (2013) Preparation of a novel electrospun polyvinyl alcohol/titanium oxide nanofiber adsorbent modified with mercapto groups for uranium(VI) and thorium(IV) removal from aqueous solution. Chem Eng J 220:161–171. https://doi.org/10.1016/j.cej.2013.01.029
43. Nilchi A, Shariati Dehaghan T, Rasouli Garmarodi S (2013) Kinetics, isotherm and thermodynamics for uranium and thorium ions adsorption from aqueous solutions by crystalline tin oxide nanoparticles. Desalination 321:67–71
44. Tedesco PH, de Rumi VB, González Quintana JA (1967) Extraction of tetravalent metals with di(2-ethylhexyl) phosphoric acid—III cerium. J Inorg Nucl Chem 29:2813–2817. https://doi.org/10.1016/0022-1902(67)80021-6
45. Bouchaud B, Balmain J, Bonnet G, Pedraza F (2012) pH-distribution of cerium species in aqueous systems. J Rare Earths 30:559–562. https://doi.org/10.1016/S1002-0721(12)60091-X
46. Alipour D, Keshtkar AR, Moosavian MA (2016) Adsorption of thorium(IV) from simulated radioactive solutions using a novel electrospun PVA/TiO_2/ZnO nanofiber adsorbent functionalized with mercapto groups: study in single and multi-component systems. Appl Surf Sci 366:19–29. https://doi.org/10.1016/j.apsusc.2016.01.049
47. Yang S, Qian J, Kuang L, Hua D (2017) Ion-imprinted mesoporous silica for selective removal of uranium from highly acidic and radioactive effluent. ACS Appl Mater Interfaces 9:29337–29344. https://doi.org/10.1021/acsami.7b09419
48. Huang Y, Zheng H, Li H, Zhang Z, Zhao C, Gou Q, Liu Y (2021) Highly effective and selective adsorption of thorium(IV) from aqueous solution using mesoporous graphite carbon nitride prepared by sol-gel template method. Chem Eng J 410:128321. https://doi.org/10.1016/j.cej.2020.128321
49. Lagergren S (1898) About the theory of so-called adsorption of soluble substances, Zur theorie der sogenannten adsorption geloster stoffe. K Sven Vetensk Handl 24:1–39
50. Negm SH, Abd El-Hamid AAM, Gado MA, El-Gendy HS (2018) Selective uranium adsorption using modified acrylamide resins. J Radioanal Nucl Chem 319:327–337
51. Washahy AR, Sakr AK, Gouda AA, Atia BM, Somaily HH, Hanfi MY, Sayyed MI, El Sheikh R, El-Sheikh EM, Radwan HA (2022) Selective recovery of cadmium, cobalt, and nickel from spent Ni-Cd batteries using Adogen® 464 and mesoporous silica derivatives. Int J Mol Sci. https://doi.org/10.3390/ijms23158677
52. Wang J, Guo X (2020) Adsorption kinetic models: physical meanings, applications, and solving methods. J Hazard Mater 390:122156. https://doi.org/10.1016/j.jhazmat.2020.122156
53. Ibrahium HA, Atia BM, Awwad NS, Nayl AA, Radwan HA, Gado MA (2022) Efficient preparation of phosphazene chitosan derivatives and its applications for the adsorption of molybdenum from spent hydrodesulfurization catalyst. J Dispersion Sci Technol 44(11):2103–2118. https://doi.org/10.1080/01932691.2022.2059508
54. Roy A, Bhattacharya J (2013) A binary and ternary adsorption study of wastewater Cd(II), Ni(II) and Co(II) by α-Fe_2O_3 nanotubes. Sep Purif Technol 115:172–179. https://doi.org/10.1016/j.seppur.2013.05.010
55. Awwad NS, Younis HM, Ibrahium HA, Atia BM, Gado MA (2024) Efficient and sustainable design of pyridyl-bis-thiourea pincer ligand-immobilised Merrifield polymer precursor for arsenic ions adsorption. Int J Environ Anal Chem. https://doi.org/10.1080/03067319.2024.2371999
56. Langmuir I (1918) The adsorption of gases on plane surfaces of glass, mica and platinum. J Am Chem Soc 40:1361–1403. https://doi.org/10.1021/ja02242a004
57. Depci T, Kul AR, Önal Y (2012) Competitive adsorption of lead and zinc from aqueous solution on activated carbon prepared from Van apple pulp: study in single- and multi-solute systems. Chem Eng J 200–202:224–236. https://doi.org/10.1016/j.cej.2012.06.077
58. Mahmoud SA, Atia BM, Abdalla M (2024) Polyvinyl alcohol-conjugated L-cysteine: a novel metal pincer for efficient heavy metal ions removal from wastewater. ChemistrySelect 9:e202401169. https://doi.org/10.1002/slct.202401169
59. Rashidi F, Sarabi RS, Ghasemi Z, Seif A (2010) Kinetic, equilibrium and thermodynamic studies for the removal of lead(II) and copper(II) ions from aqueous solutions by nanocrystalline TiO_2. Superlattices Microstruct 48:577–591. https://doi.org/10.1016/j.spmi.2010.09.011
60. Mittal A, Kaur D, Mittal J (2009) Batch and bulk removal of a triarylmethane dye, fast green FCF, from wastewater by adsorption over waste materials. J Hazard Mater 163:568–577
61. Sarı A, Tuzen M (2009) Kinetic and equilibrium studies of biosorption of Pb(II) and Cd(II) from aqueous solution by macrofungus (*Amanita rubescens*) biomass. J Hazard Mater 164:1004–1011. https://doi.org/10.1016/j.jhazmat.2008.09.002
62. Gado MA (2018) Sorption of thorium using magnetic graphene oxide polypyrrole composite synthesized from natural source. Sep Sci Technol 53(13):2016–2033. https://doi.org/10.1080/01496395.2018.1443130
63. Ibrahium HA, Gado MA, Awwad NS, Fathy WM (2021) Selective separation of yttrium and uranium from xenotime concentrate. Z Anorg Allg Chem 647:1568. https://doi.org/10.1002/zaac.202100118
64. Zhang J, Wang L, Zhong A, Huang G, Wu F, Li D, Teng M, Wang J, Han D (2019) Deep red PhOLED from dimeric salophen Platinum(II) complexes. Dyes Pigm 162:590–598. https://doi.org/10.1016/j.dyepig.2018.10.053
65. Abd El-Magied MO (2023) High-efficiency recovery of cerium ions from monazite leach liquor by polyamines and polycarboxylates chitosan sorbents prepared from marine industrial wastes. Int J Biol Macromol 243:125243. https://doi.org/10.1016/j.ijbiomac.2023.125243
66. Rizk S (2005) Chemical studies related to redox processes in uranium–cerium separation. Master's thesis, Zagazig University, Faculty of Science, Chemistry Department
67. Zhang J, Ju X, Wu ZY, Liu T, Hu TD, Xie YN, Zhang ZL (2001) Structural characteristics of cerium oxide nanocrystals prepared by the microemulsion method. Mater Chem Phys 13:4192–4197. https://doi.org/10.1021/cm010235p
68. Alotaibi AM, Ismail AF (2022) Modification of clinoptilolite as a robust adsorbent for highly-efficient removal of thorium (IV) from aqueous solutions. Int J Environ Res Public Health 19:13774. https://doi.org/10.3390/ijerph192113774
69. Chen K, Zornes A, Bababrik R, Crouch J, Alvarez W, Wulfers M, Resasco D, Wang B, Crossley S, White JL (2021) First-formed framework species and phosphate structure distributions in phosphorus-modified MFI zeolites. J Phys Chem C 126:227–238. https://doi.org/10.1021/acs.jpcc.1c08448

70. Albayari M, Nazal MK, Khalili FI, Nordin N, Adhan R (2021) Biochar derived from *Salvadora persica* branches biomass as low-cost adsorbent for removal of uranium (VI) and thorium (IV) from water. J Radioanal Nucl Chem 328:669–678. https://doi.org/10.1007/s10967-021-07667-2
71. Huang Y, Zheng H, Li H, Zhang Z, Zhao C, Gou Q, Liu Y (2021) Highly effective and selective adsorption of thorium(IV) from aqueous solution using mesoporous graphite carbon nitride prepared by sol–gel template method. Chem Eng J 410:128321. https://doi.org/10.1016/j.cej.2020.128321
72. Kaynar UH, Çam Kaynar S, Ekdal Karali E, Ayvacıkli M, Can N (2021) Adsorption of thorium (IV) ions by metal ion doped ZnO nanomaterial prepared with combustion synthesis: empirical modelling and process optimization by response surface methodology (RSM). Appl Radiat Isot 178:109955. https://doi.org/10.1016/j.apradiso.2021.109955
73. Huang G, Chen Z, Wang L et al (2016) Removal of thorium(IV) from aqueous solution using magnetic ion-imprinted chitosan resin. J Radioanal Nucl Chem 310:1265–1272. https://doi.org/10.1007/s10967-016-4993-0
74. Hamza M, Wei Y, Khalafalla M, Abed N, Fouda A, Elwakeel K, Guibal E (2022) U(VI) and Th(IV) recovery using silica beads functionalized with urea- or thiourea-based polymers—application to ore leachate. Sci Total Environ 821:153184
75. Oter Ç, Zorer OS (2021) Adsorption behaviours of Th(IV) and U(VI) using nitric acid (HNO3) modified activated carbon: equilibrium, thermodynamic and kinetic studies. Int J Environ Anal Chem 101(14):1950–1965. https://doi.org/10.1080/03067319.2019.1691184
76. Gado M, Atia B, Cheira M, Abdou A (2019) Thorium ions adsorption from aqueous solution by amino naphthol sulphonate coupled chitosan. Int J Environ Anal Chem 101:1419–1436. https://doi.org/10.1080/03067319.2019.1683552
77. Gore P, Khurana L, Siddique S, Panicker A, Kandasubramanian B (2018) Ion-imprinted electrospun nanofibers of chitosan/1-butyl-3-methylimidazolium tetrafluoroborate for the dynamic expulsion of thorium (IV) ions from mimicked effluents. Environ Sci Pollut Res 25:3320–3334. https://doi.org/10.1007/s11356-017-0618-6
78. Karimi M, Milani SA, Abolgashemi H (2016) Kinetic and isotherm analyses for thorium (IV) adsorptive removal from aqueous solutions by modified magnetite nanoparticle using response surface methodology (RSM). J Nucl Mater 479:174–183. https://doi.org/10.1016/j.jnucmat.2016.07.020
79. Varsihini JS, Das D, Das N (2014) Optimization of parameters for cerium(III) biosorption onto biowaste materials of animal and plant origin using 5-level Box-Behnken design: equilibrium, kinetic, thermodynamic and regeneration studies. J Rare Earths 32:745
80. Pereao O, Laatikainen K, Bode-Aluko C, Kochnev I, Fatoba O, Nechaev AN, Petrik L (2020) Adsorption of Ce^{3+} and Nd^{3+} by diglycolic acid functionalized electrospun polystyrene nanofiber from aqueous solution. Sep Purif Technol 233:116059. https://doi.org/10.1016/j.seppur.2019.116059
81. Lee YR, Yu K, Ravi S, Ahn W-S (2018) Selective adsorption of rare earth elements over functionalized Cr-MIL-101. ACS Appl Mater Interfaces 10:23918–23927. https://doi.org/10.1021/acsami.8b07130
82. Li XJ, Yan CJ, Luo WJ, Gao Q, Zhou Q, Liu C, Zhou S (2016) Exceptional cerium (III) adsorption performance of poly(acrylic acid) brushes-decorated attapulgite with abundant and highly accessible binding sites. Chem Eng J 284:333–342. https://doi.org/10.1016/j.cej.2015.09.003
83. Zhou S, Li X, Shi Y, Alshameri A, Yan C (2015) Preparation, characterization, and Ce(III) adsorption performance of poly(allylamine)/silica composite. Desalin Water Treat 56:1321–1334. https://doi.org/10.1080/19443994.2014.944221
84. Awual MR, Hasan MM, Shahat A, Naushad M, Shiwaku H, Yaita T (2015) Investigation of ligand immobilized nano-composite adsorbent for efficient cerium(III) detection and recovery. Chem Eng J 265:210–218. https://doi.org/10.1016/j.cej.2014.12.052
85. Vijayaraghavan K, Sathishkumar M, Balasubramanian R (2010) Biosorption of lanthanum, cerium, europium and ytterbium by a brown marine alga *Turbinaria conoides*. Ind Eng Chem Res 49:4405. https://doi.org/10.1021/ie1000373
86. Hendy MA, Kashar TI, Allam EI, Gado MA, Yahia NS, Cheira MF (2024) Thorium ions elimination from its solution utilizing the assembled sulfosuccinic acid/polyvinyl alcohol/polyamide. Mater Today Commun 40:109633. https://doi.org/10.1016/j.mtcomm.2024.109633
87. Iftekhar S, Srivastava V, Sillanpää M (2017) Synthesis and application of LDH intercalated cellulose nanocomposite for separation of rare earth elements (REEs). Chem Eng J 309:130–139. https://doi.org/10.1016/j.cej.2016.10.028
88. Zare-Dorabei R, Jalalat V, Tadjarodi A (2016) Central composite design optimization of Ce(III) ion removal from aqueous solution using modified SBA-15 mesoporous silica. New J Chem 40:5128–5134. https://doi.org/10.1039/C6NJ00239K

Publisher's Note Springer Nature remains neutral with regard to jurisdictional claims in published maps and institutional affiliations.